Surrogate-enhanced higher order eigenstrain-based reduced order homogenization for polycrystal plasticity

Aslan Nasirov and Caglar Oskay*
Department of Civil and Environmental Engineering
Vanderbilt University
Nashville, TN

Abstract

Reduced-order models (ROMs) are frequently employed within concurrent multiscale frameworks to enhance the efficiency of nonlinear simulations and to mitigate the substantial computational expense associated with direct nonlinear homogenization schemes. Among these, transformation field analysis (TFA)-based ROMs have gained particular prominence due to their reliance on linear elastic simulations for model construction and their characteristically low dimensionality. However, extensive studies have demonstrated that these models often exhibit an artificially stiff response when applied across a broad spectrum of materials. In the present study, a higher order eigenstrain homogenization scheme is presented to mitigate the overly stiff response predicted by these models. Another challenge with the incorporation of nonuniform or higher order basis within models based on TFA is the expensive integration of the constitutive response due to nonuniform fields. A novel approach to compute these integrals is established that reduces the number of integration parameters over complex three-dimensional domains without additional spatial constraints. It is demonstrated that the linear modes can soften the elasto-plastic response and that the proposed integration method achieves approximately an order-of-magnitude improvement in computational efficiency compared to brute-force integration over a background mesh.

Keywords: Computational homogenization; Reduced order modeling; Multiscale modeling; Crystal plasticity

*Corresponding author address: VU Station B#351831, 2301 Vanderbilt Place, Nashville, TN 37235. Email: caglar.oskay@vanderbilt.edu

1 Introduction

Accurate modeling of the nonlinear mechanical behavior of structures made of advanced materials with complex microstructures such as metal alloys, composites, and architected materials requires the development and application of multiscale methods [1]. A variety of such methods are available (e.g., computational homogenization [2], variational multiscale enrichment [3], multiscale finite elements [4, 5]) to address specific classes of problems and material systems. For scale separable problems, a classical strategy is the computational homogenization (CH) method, which requires solving coupled nonlinear boundary value problems (BVPs) at both the macroscale and microscale using finite elements or other numerical techniques [6, 7, 8]. CH has been successfully applied to investigate various multiscale phenomena, such as the influence of microscale and mesoscale defects on the multiscale response of additively manufactured composites [9], the role of microstructural morphology in the response of heterogeneous interfaces [10], among many others.

The computational cost of CH implementations is typically high and significant computational resources for simulating realistic-sized structures are required. This challenge has limited its broader adoption. To address this limitation, reduced order models (ROMs) are employed by approximating the microscale response without resorting to full-field methods such as the finite element method (FEM) or the spectral method. A variety of ROM approaches have been developed in the literature including transformation field analysis (TFA) [11, 12], nonuniform TFA (NTFA) [13, 14, 15, 16, 17] and its extensions [18, 19, 20], numerical potentials [21], self-consistent clustering analysis [22], eigendeformation methods [23, 24, 25, 26], eigenstrain-based reduced order homogenization (EHM) [27, 28, 29, 30], deep material network [31] and proper orthogonal decomposition (POD) [32, 33, 34], with continuing developments exploring hybrid physics-informed and machine learning frameworks [35, 36].

ROM frameworks generally consist of two distinct stages: (1) "offline" model construction (or training); and (2) "online" execution. During the offline stage (i.e., prior to the execution of the multiscale simulation), the ROM is constructed based on a pre-defined set of microstructure simulations. Model construction for some ROM approaches such as the NTFA, POD, and machine learning-based surrogate models involves conducting a comprehensive set of nonlinear and history-dependent microscale simulations subjected to a wide range of loading paths. In EHM, a predefined set of linear elastic simulations independent of the loading path is needed. During the online stage, the microscale BVP is replaced by the ROM, a nonlinear algebraic system of equations posed over a coarse approximation space spanned by a small number of basis functions. This substitution leads to significant computational efficiency, as the reduced system is of much lower dimension and can be efficiently coupled with the macroscopic solver.

While EHM and other TFA-based ROMs offer significant efficiency gains for nonlinear multiscale simulations, they can exhibit limitations in capturing inelastic responses for certain loading paths and microstructures. A common issue is an artificially stiff response compared to direct numerical simulations, a phenomenon reported in multiple prior studies [37, 28, 38]. The prediction error is generally more severe in high phase-contrast materials (e.g., carbon fiber reinforced polymer composites) than in lower phase-contrast materials such as polycrystalline metals. To address this shortcoming, several strategies have been explored, including ROM refinement based on phase subpartitioning [23, 39, 40, 22], online ROM reconstruction using instantaneous moduli [37, 30, 41], and the use of nonuniform basis functions [42, 14, 19, 18]. Incorporating the instantaneous moduli yields substantial improvement for high-phase-contrast microstructures but offers limited benefit in low-phase-contrast cases and requires online reconstruction, which is computationally expensive. A straightforward alternative is to subdivide each phase domain into smaller reduced-order parts, analogous to h-refinement in finite element analysis. However, meaningful accuracy gains generally require many subpartitions, even with advanced algorithms, as shown for both polycrystalline [25] and composite [43] microstructures. In contrast, the incorporation of nonuniform basis functions has demonstrated significant performance improvements, particularly when the basis functions are well chosen.

A broad range of basis constructions has been explored for composite materials, including piecewise-uniform [11, 12], piecewise-polynomial [19], mixed discretizations [15], and globally nonuniform bases [14]. Michel and Suquet [14] introduced the use of globally nonuniform basis functions in the NTFA framework, deriving them from nonlinear full-field microstructure simulations. Similar strategies were later explored by Fritzen et al. [18] and by Beel and Fish [44] who advocated using a small set of six unidirectional loading simulations for the construction of the reduced basis. These approaches generally achieve high accuracy, particularly when the applied loading remains close to that used in constructing the basis functions. Sepe et al. [19] proposed analytical basis functions to avoid the cost of such a priori nonlinear simulations, demonstrating their effectiveness for two-dimensional elastoplastic composites. Covezzi et al. [15] developed a mixed discretization for two-dimensional elastoviscoplastic composites, employing divergence-free stress bases alongside piecewise-linear strain and inelastic-strain functions. An additional challenge associated with the use of nonuniform basis functions is integrating the nonlinear constitutive law efficiently [19]. This challenge has been tackled by using reduced version of the constitutive model [14], Gauss point clustering [45], evolving Gauss points [44], second order Taylor expansions [46], and empirical quadrature method [47].

The focus of the present study is achieving consistent improvement in ROM accuracy compared to the classical EHM approach in the context of low-phase-contrast polycrystalline materials regardless

of loading and microstructural morphology. We employ polynomial-type higher-order basis functions to achieve this consistent accuracy improvement and accurately capture intragrain heterogeneity. First, a set of microscale equilibrium problems for higher-order basis functions is derived to describe the offline stage. For the online stage, reduced order versions of the constitutive equations are derived using variational principles which include a computationally intensive integration of the viscoplastic flow rule. We reformulate the integration problem and propose a machine-learning-based surrogate model that performs constitutive integration more efficiently. The primary contributions of this work are twofold: (i) the application of the ROM enhanced with higher-order basis functions to three-dimensional polycrystal plasticity problems, and (ii) the development of a novel surrogate approach to significantly reduce integration time.

The remainder of this manuscript is organized as follows: The EHM methodology is briefly summarized and the mathematical formulation for the proposed higher order model is derived and discussed in Section 2. Starting with a brief reintroduction of the key equations from classical EHM, Section 2.1 presents the higher-order discretization. Sections 2.2 and 2.3 use this discretization to derive the reduced constitutive law and evolution equations. Section 2.4 introduces the surrogate framework, followed by the offline stage comprising the influence-function problems in Section 2.5. Section 2.6 concludes with the description of the ROM algorithm. Numerical experiments performed to assess the accuracy of the proposed method are discussed in Section 3. Conclusions are presented in Section 4.

The following notation is used unless otherwise stated. Tensor fields are provided in Cartesian coordinates and are denoted as italic lightface letters (A_{ijkl} or σ_{ij}), in indicial notation, or in boldface italic, ($\boldsymbol{A}$ or $\boldsymbol{\sigma}$), in tensor notation. Scalars are denoted by lightface letters, α without indices. Parentheses in the subscript indicate the symmetric part of the tensor. A comma in the indices indicates partial spatial derivative. The top right superscript is used as a descriptor. The bottom left subscript denotes time increment. Overbar indicates macroscopic quantity averaged over the microstructural domain while overhead dot indicates time derivative. N_{ph} denotes number of grains in the polycrystal, N_{m} the number of modes per grain, and N_{Voigt} the number of Voigt components (six in three-dimensional simulations).

2 Higher order EHM (HEHM)

Consider a macroscopic domain, $\Omega \subset \mathbb{R}^3$, that is made of a periodic polycrystalline microstructural volume, $\Theta \subset \mathbb{R}^3$. The material constituents that occupy the domain behave in an inelastic manner,

which is idealized using the small strain theory and additive decomposition of the total strain

$$\sigma_{ij}(\boldsymbol{x},\boldsymbol{y},t) = L_{ijkl}(\boldsymbol{y})\left[\varepsilon_{kl}(\boldsymbol{x},\boldsymbol{y},t) - \mu_{kl}(\boldsymbol{x},\boldsymbol{y},t)\right] \tag{1}$$

where $\boldsymbol{\sigma}$ is the stress tensor, $\boldsymbol{L}$ the tensor of elastic moduli, $\boldsymbol{\varepsilon}$ the total strain, and $\boldsymbol{\mu}$ the inelastic strain. $\boldsymbol{x}$ denotes the macroscopic position vector defined over Ω, $\boldsymbol{y}$ is the microscopic position vector defined over Θ, and t is the time coordinate. The strain field over the microstructural volume at an arbitrary position $\boldsymbol{x}$ of the macroscale structure is decomposed as

$$\varepsilon_{ij}(\boldsymbol{x},\boldsymbol{y},t) = \overline{\varepsilon}_{ij}(\boldsymbol{x},t) + \tilde{\varepsilon}_{ij}(\boldsymbol{x},\boldsymbol{y},t) \tag{2}$$

where $\overline{\boldsymbol{\varepsilon}}$ is the macroscale strain tensor, and $\tilde{\boldsymbol{\varepsilon}}$ is the zero-mean microscale strain perturbation over the microstructural volume. The strain perturbation field is then expanded as follows [28]

$$\tilde{\varepsilon}_{ij}(\boldsymbol{x},\boldsymbol{y},t) = H_{(i,j)mn}(\boldsymbol{y})\overline{\varepsilon}_{mn}(\boldsymbol{x},t) + \int_{\Theta} h_{(i,j)mn}(\boldsymbol{y},\hat{\boldsymbol{y}})\mu_{mn}(\boldsymbol{x},\hat{\boldsymbol{y}},t)d\hat{\boldsymbol{y}} \tag{3}$$

where $\boldsymbol{H}(\boldsymbol{y})$ and $\boldsymbol{h}(\boldsymbol{y},\hat{\boldsymbol{y}})$ are elastic and phase influence functions, respectively.

2.1 Field-discretization

The ansatz in Eq. 3 forms the foundation of the EHM model. In the classical EHM formulation [28], the spatial distribution of the inelastic strain and the stress fields over the microstructural volume is approximated as piecewise-uniform over prescribed subdomains of Θ. In this section, we propose an extension of this approximation by including a hierarchy of higher-order basis functions. The goal of this extension is to monotonically increase the accuracy of a ROM prepared by a given set of basis functions by including additional higher-order basis functions from the hierarchy. Let $\{\Theta^{(\alpha)} \in \Theta \,|\, \alpha = 1,\ldots,N_{\mathrm{ph}}\}$ denote a partition of Θ. We proceed with the following discretization of the inelastic strain and stress fields

$$\mu_{ij}(\boldsymbol{x},\boldsymbol{y},t) = \sum_{\alpha=1}^{N_{\mathrm{ph}}}\sum_{p=1}^{N_{\mathrm{m}}} N^{(\alpha,p)}(\boldsymbol{y})\mu_{ij}^{(\alpha,p)}(\boldsymbol{x},t) \tag{4}$$

$$\sigma_{ij}(\boldsymbol{x},\boldsymbol{y},t) = \sum_{\alpha=1}^{N_{\mathrm{ph}}}\sum_{p=1}^{N_{\mathrm{m}}} N^{(\alpha,p)}(\boldsymbol{y})\sigma_{ij}^{(\alpha,p)}(\boldsymbol{x},t) \tag{5}$$

where $N^{(\alpha,p)}$ is a basis function associated with part α and mode p, and $\boldsymbol{\mu}^{(\alpha,p)}$ and $\boldsymbol{\sigma}^{(\alpha,p)}$ are the corresponding eigenstrain and stress coefficients, respectively.

In the present study, polynomial basis functions are used following the ideas proposed in Ref. [19]. The basis functions are chosen such that they have compact support within their parts, i.e., $N^{(\alpha,p)}(\boldsymbol{y} = \Theta \cap \overline{\Theta^{(\alpha)}}) = 0$. This property of the basis functions enables partial localization of the constitutive equations; for instance, the Schmid tensor remains constant within a grain and does not require additional treatment. Furthermore, the basis functions are constructed to satisfy orthonormality condition given as

$$\int_{\Theta^{(\beta)}} N^{(\beta,p)}(\boldsymbol{y})\, N^{(\beta,q)}(\boldsymbol{y}) d\boldsymbol{y} = \begin{cases} 0, & p \neq q, \\ 1, & p = q. \end{cases} \tag{6}$$

Orthonormalizing the basis functions beforehand simplifies the numerical implementation and improves conditioning of the reduced system as elaborated in Section 2.3.

Construction of the orthonormal basis functions can be achieved by the Gram-Schmidt orthonormalization procedure. For consistency with the classical EHM formulation, the first basis function is constrained to be constant within its corresponding part: $\tilde{N}^{(\beta,1)} = 1$. To generate higher-order basis functions based on polynomial expansions, we begin by selecting a set of linearly independent, non-orthogonal functions. For instance, the set of linear polynomials are

$$\tilde{N}^{(\beta,2)} = y_1, \tilde{N}^{(\beta,3)} = y_2, \tilde{N}^{(\beta,4)} = y_3; \qquad \boldsymbol{y} \in \Theta^{(\beta)}. \tag{7}$$

The orthonormalized basis functions are then obtained recursively via the Gram–Schmidt process, with the first mode given by

$$N^{(\beta,1)}(\boldsymbol{y}) = \frac{\tilde{N}^{(\beta,1)}(\boldsymbol{y})}{\sqrt{\int_{\Theta^{(\beta)}} \tilde{N}^{(\beta,1)}(\boldsymbol{y}) \tilde{N}^{(\beta,1)}(\boldsymbol{y}) d\boldsymbol{y}}} \tag{8}$$

and the rest of the modes given by

$$\hat{N}^{(\beta,p)}(\boldsymbol{y}) = \tilde{N}^{(\beta,p)}(\boldsymbol{y}) - \sum_{q=1}^{p-1} \left(\frac{\int_{\Theta^{(\beta)}} \tilde{N}^{(\beta,p)}(\boldsymbol{y}) N^{(\beta,q)}(\boldsymbol{y}) d\boldsymbol{y}}{\int_{\Theta^{(\beta)}} N^{(\beta,q)}(\boldsymbol{y}) N^{(\beta,q)}(\boldsymbol{y}) d\boldsymbol{y}} \right) N^{(\beta,q)}(\boldsymbol{y}) \tag{9}$$

$$N^{(\beta,p)}(\boldsymbol{y}) = \frac{\hat{N}^{(\beta,p)}(\boldsymbol{y})}{\sqrt{\int_{\Theta^{(\beta)}} \hat{N}^{(\beta,p)}(\boldsymbol{y}) \hat{N}^{(\beta,p)}(\boldsymbol{y}) d\boldsymbol{y}}}. \tag{10}$$

This approach is conceptually analogous to p-refinement in finite element analysis, where the order of interpolation within each element is increased to more accurately capture field nonuniformities. As an illustrative example, the functions $\tilde{N}^{(\beta,1)} = 1, \tilde{N}^{(\beta,2)} = y_1, \tilde{N}^{(\beta,3)} = y_2, \tilde{N}^{(\beta,4)} = y_1^2$ are plotted over

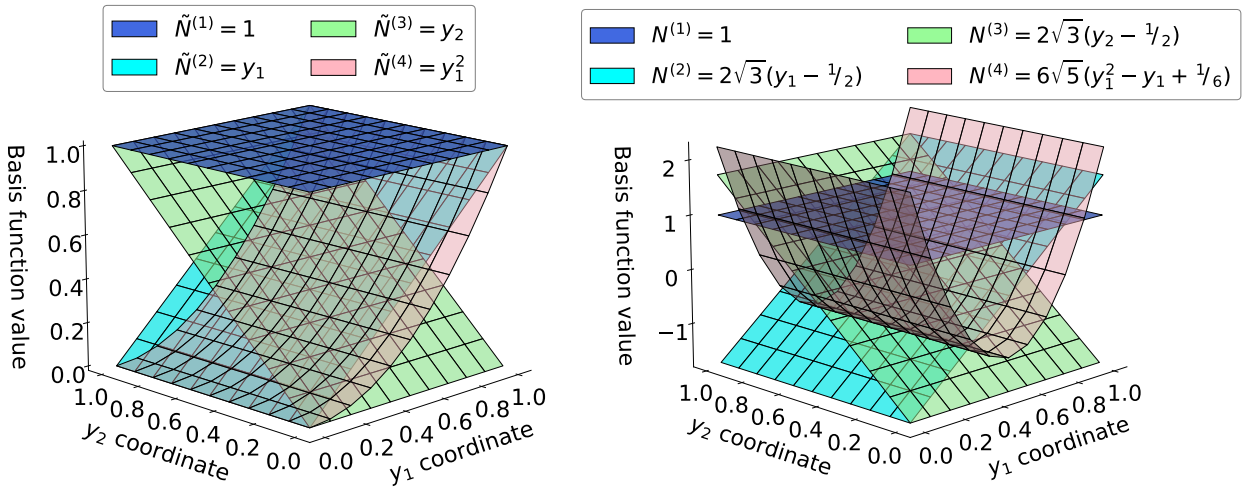

(a) (b)

Figure 1: (a) Initial (non-orthonormal) basis functions over a square domain $[0, 1]^2$ in 2D and (b) modified basis functions after orthonormalization.

the unit square domain $[0, 1]^2$ in Figure 1 both before and after orthonormalization, to demonstrate the transformation.

2.2 Reduced Constitutive Equations

In this section, the constitutive relations are projected onto the reduced basis introduced earlier to obtain a finite-dimensional representation of the microscale response. The resulting reduced constitutive equations introduce the localization and interaction tensors that encode the mechanical interactions within and between parts, and these tensors form the central building blocks of the ROM used in the subsequent development. Combining the prescribed discretization in Eq. 4 with Eqs. 1, 2, and 3 yields the following expression for the stress

$$\sigma_{ij}(\boldsymbol{x}, \boldsymbol{y}, t) = L_{ijkl}(\boldsymbol{y}) \Big[\overline{\varepsilon}_{kl}(\boldsymbol{x}, t) + H_{(k,l)mn}(\boldsymbol{y})\, \overline{\varepsilon}_{mn}(\boldsymbol{x}, t) + \sum_{\alpha=1}^{N_{\text{ph}}} \sum_{p=1}^{N_{\text{m}}} \left(h_{(k,l)mn}^{(\alpha,p)}(\boldsymbol{y}) - N^{(\alpha,p)}(\boldsymbol{y})\, I_{klmn} \right) \mu_{mn}^{(\alpha,p)}(\boldsymbol{x}, t) \Big] \tag{11}$$

where $\boldsymbol{h}^{(\alpha,p)}(\boldsymbol{y}) = \int_{\Theta} \boldsymbol{h}(\boldsymbol{y}, \hat{\boldsymbol{y}}) N^{(\alpha,p)}(\hat{\boldsymbol{y}}) d\hat{\boldsymbol{y}}$ is the integrated phase influence function. Substituting discretizations in Eq. 5 into Eq. 11, premultiplying with $N^{(\beta,q)}$, and integrating over $\Theta^{(\beta)}$ we get

$$M_{klij}^{(\beta)}\sigma_{ij}^{(\beta,q)} = A_{klmn}^{(\beta,q)}\overline{\varepsilon}_{mn} + \sum_{\alpha=1}^{N_{\text{ph}}}\sum_{p=1}^{N_{\text{m}}} P_{klmn}^{(\beta\alpha,qp)}\mu_{mn}^{(\alpha,p)} - \mu_{kl}^{(\beta,q)} \tag{12}$$

where

$$A_{klmn}^{(\beta,q)} = \int_{\Theta^{(\beta)}} N^{(\beta,q)}(\boldsymbol{y})\left[I_{klmn} + H_{(k,l)mn}(\boldsymbol{y})\right] d\boldsymbol{y} \tag{13}$$

$$P_{klmn}^{(\beta\alpha,qp)} = \int_{\Theta^{(\beta)}} N^{(\beta,q)}(\boldsymbol{y}) h_{(k,l)mn}^{(\alpha,p)}(\boldsymbol{y}) d\boldsymbol{y} \tag{14}$$

in which $\boldsymbol{M}^{(\beta)} = \boldsymbol{L}^{(\beta)^{-1}}$, $\boldsymbol{L}^{(\beta)}$ is the part-averaged stiffness tensor, $\boldsymbol{A}^{(\beta,q)}$ is the localization tensor, and $\boldsymbol{P}^{(\beta\alpha,qp)}$ the interaction tensor representing interactions between mode q in part β and mode p in part α.

2.3 Reduced Evolution Equations

Equation 12 establishes a linear mapping between the stress and inelastic strain coefficients, both of which are unknown. In order to close the system, the constitutive laws that govern the viscoelasto-plastic response of the crystals within the microstructure are invoked. Various forms of evolution equations have been previously proposed to describe the nonlinear behavior of polycrystalline materials (e.g., [48, 49, 50]). In this study, we adopt a dislocation-glide based phenomenological crystal plasticity model. The flow rule [51, 28] at a material point is given by

$$\dot{\mu}_{ij} = \sum_{s=1}^{N_{\text{ss}}} \dot{\gamma}_0 \left[\frac{|\tau^s|}{g^s}\right]^{1/n} \text{sign}(\tau^s) Z_{ij}^s \tag{15}$$

where $\boldsymbol{Z}^s$ is the Schmid tensor associated with a slip system s, $\dot{\gamma}_0$ is the reference self-shearing rate, n is the rate sensitivity parameter, g^s is the slip system strength, and $\tau^s = \boldsymbol{\sigma} : \boldsymbol{Z}^s$ is the resolved shear stress over the s^{th} slip system, and N_{ss} is the number of slip systems in the lattice. The hardening rule [52, 53] is given by

$$\dot{g}^s = h_0 \left[\frac{g_{\text{sa}} - g^s}{g_{\text{sa}} - g_0}\right] \sum_{r=1}^{N_{\text{ss}}} |\dot{\gamma}_0 \left[\frac{|\tau^r|}{g^r}\right]^{1/n} \text{sign}(\tau^r)| \tag{16}$$

where h_0 is reference self-hardening, g_0 is the initial strength of a slip system, and g_{sa} is saturation strength.

When the basis functions of the reduced order model are piecewise uniform (e.g., in the classical EHM approach), the flow and hardening rules can be directly expressed in terms of stress and inelastic strain coefficients, as well as similarly defined hardening variable coefficients [28]. Hence, the flow and hardening evolution rules for the reduced order coefficients are of the same form as the point-wise evolution equations defined in Eqs. 15 and 16. However, when basis functions are nonuniform, the constitutive laws cannot be satisfied exactly at every point within a grain, while also considering the reduced order approximations for the stress and inelastic strain fields (i.e., Eqs. 5 and 4). This is because the nonlinearity in the constitutive laws result in a spatial distribution of the fields within the part that is inconsistent with the polynomial basis. The approach in this paper is to construct a reduced-flow rule where Eq. 15 is satisfied in a weak sense. Consider the following weak form of the flow rule

$$\int_{\Theta^{(\beta)}} N^{(\beta,p)}(\boldsymbol{y}) \left(\dot{\mu}_{ij}(\boldsymbol{y}) - \sum_{s=1}^{N_{\text{ss}}} \dot{\gamma}_0 \left[\frac{|\tau^s(\boldsymbol{y})|}{g^s(\boldsymbol{y})} \right]^{1/n} \text{sign}(\tau^s(\boldsymbol{y})) Z_{ij}^s \right) d\boldsymbol{y} = 0. \tag{17}$$

Substituting the reduced order discretizations of the stress and inelastic strain fields result in the following expression

$$\dot{\mu}_{ij}^{(\beta,p)} = \sum_s \dot{\gamma}^{(\beta,p),s} Z_{ij}^{(\beta),s} \tag{18}$$

where

$$\dot{\gamma}^{(\beta,p),s} = \dot{\gamma}_0 \int_{\Theta^{(\beta)}} N^{(\beta,p)}(\boldsymbol{y}) \left[\frac{\left| \sum_{q=1}^{N_{\text{m}}} N^{(\beta,q)}(\boldsymbol{y}) \tau^{(\beta,q),s} \right|}{g^s(\boldsymbol{y})} \right]^{1/n} \text{sign}\left(\sum_{q=1}^{N_{\text{m}}} N^{(\beta,q)}(\boldsymbol{y}) \tau^{(\beta,q),s} \right) \, d\boldsymbol{y} \tag{19}$$

and $\dot{\gamma}^{(\beta,p),s}$ is the reduced plastic slip rate for grain β, mode p and slip system s, and $\tau^{(\beta,p),s} = \boldsymbol{\sigma}^{(\beta,p)} : \boldsymbol{Z}^{(\beta),s}$ is the resolved shear stress coefficient corresponding to mode p. The right-hand side of Eq. 19 could be numerically integrated for a given input of stress coefficients, $\boldsymbol{\sigma}^{(\beta,p)}$, and hardening coefficients, $g^{(\beta,p),s}$. Similar procedure is applied to construct a reduced hardening rule using Eq. 16.

Orthonormalizing the basis functions in advance eliminates cross-mode coupling terms and significantly simplifies the inversion required on the left-hand sides of Eqs. 12 and 18. Without orthonormalization, the reduced evolution equations retain all cross terms, leading to coupled systems of the form

$$\sum_{q=1}^{N_{\text{m}}} C_{ijkl}^{(\beta,pq)} \dot{\mu}_{kl}^{(\beta,q)} = \sum_{s=1}^{N_{\text{ss}}} \dot{\gamma}^{(\beta,p),s} Z_{ij}^{(\beta),s} \tag{20}$$

where

$$C_{ijmn}^{(\beta,pq)} = \int_{\Theta^{(\beta)}} N^{(\beta,p)}(\boldsymbol{y}) I_{ijmn} N^{(\beta,q)}(\boldsymbol{y}) d\boldsymbol{y} \tag{21}$$

denotes the inner product between modes p and q. In the absence of orthonormality, $\boldsymbol{C}^{(\beta,pq)}$ is generally dense, and each mode is coupled to all others, increasing both algebraic complexity and computational cost.

2.4 Surrogate integration

Accurate integration of Eq. 18 has a substantive effect on the overall accuracy of the reduced model predictions as demonstrated in Section 3. However, direct numerical integration of this term accurately over a complex three-dimensional microstructure is computationally expensive. This difficulty is particularly pronounced when the exponent n is small, as the integrand becomes highly nonlinear and requires a dense set of quadrature points for accurate evaluation. As discussed in the literature review, several algorithms have been proposed to reduce the number of quadrature points within each grain. A key limitation of most existing approaches is the inherent requirement that quadrature points lie strictly within the integration domain. This constraint is difficult to enforce for arbitrary three-dimensional geometries. We propose a new procedure that converts the integration problem into an interpolation problem, thereby relaxing the geometric constraint and enabling efficient evaluation over complex grain shapes. Consider a normalized resolved shear stress, $\tau_{\text{norm}}^{(\beta,p),s}$, that is given by

$$\tau_{\text{norm}}^{(\beta,p),s} = \frac{\tau^{(\beta,p),s}}{\tau_{\text{max}}^{(\beta),s}} \in [-1, 1] \tag{22}$$

where $\tau_{\text{max}}^{(\beta),s} = \tau^{(\beta,p^\star),s}$ and $p^\star = \text{argmax}_p(|\tau^{(\beta,p),s}|)$. Without loss of generality, we assume hardening has only the average mode for simplicity. The integral for computing the reduced plastic slip rates (Eq. 19) is expressed as follows

$$\dot{\gamma}^{(\beta,p),s} = \dot{\gamma}_0 \left[\frac{|\tau_{\text{max}}^{(\beta),s}|}{g^{(\beta),s}} \right]^{1/n} \text{sign}(\tau_{\text{max}}^{(\beta),s}) I^{(\beta,p)}(\boldsymbol{\tau}_{\text{norm}}^{(\beta),s}) \tag{23}$$

where

$$I^{(\beta,p)}(\tau^{(\beta),s}_{\text{norm}}) = \int_{\Theta^{(\beta)}} N^{(\beta,p)}(\boldsymbol{y}) \left[\left| \sum_{q=1} N^{(\beta,q)}(\boldsymbol{y}) \tau^{(\beta,q),s}_{\text{norm}} \right| \right]^{1/n} \text{sign}(\sum_{q=1} N^{(\beta,q)}(\boldsymbol{y}) \tau^{(\beta,q),s}_{\text{norm}}) d\boldsymbol{y} \tag{24}$$

and $\tau^{(\beta),s}_{\text{norm}}$ indicates normalized resolved shear stresses over the modes combined into an array form. For given coefficients $\tau^{(\beta),s}_{\text{norm}}$, the integral $I^{(\beta,p)}(\tau^{(\beta),s}_{\text{norm}})$ can be computed using, for example, composite integration rule over a background grid. This allows us to use interpolation methods over the $[-1,1]^{N_{\text{m}}}$ space without dealing with the spatial constraints over subdomains within the microstructure. Depending on the number of modes N_{m}, this space could be classified as hyper-dimensional. Various methods can be used to interpolate functions in these spaces including sparse grids [54] or high-dimensional model representation (HDMR) methods [55]. In the present work, we employ neural-network–based surrogates due to their flexibility in approximating nonlinear mappings as detailed in Section 3.5.

2.5 Influence function problems

Before proceeding to the complete algorithm, the method of computing influence functions, $\boldsymbol{H}$ and $\boldsymbol{h}^{(\alpha,p)}$, appearing in Eqs. 13 and 14 must be specified. Substituting the stress expression from Eq. 11 into the microscale equilibrium condition $\nabla \cdot \boldsymbol{\sigma} = 0$ over the microstructural volume yields

$$\begin{aligned} \Big\{ L_{ijkl}(\boldsymbol{y}) \big[I_{klmn} + H_{(k,l)mn}(\boldsymbol{y}) \big] \overline{\varepsilon}_{mn} + \\ + \sum_{\alpha=1}^{N_{\text{ph}}} \sum_{q=1}^{N_{\text{m}}} L_{ijkl}(\boldsymbol{y}) \big[-N^{(\alpha,q)}(\boldsymbol{y})\, I_{klmn} + h^{(\alpha,q)}_{(k,l)mn}(\boldsymbol{y}) \big] \mu^{(\alpha,q)}_{mn} \Big\}_{,j} = 0. \end{aligned} \tag{25}$$

Considering the microscale equilibrium (Eq. 25) defined in the absence of any inelastic strain leads to following influence function problems (IFPs)

$$\big[L_{ijkl}(\boldsymbol{y}) \left[I_{klmn} + H_{(k,l)mn}(\boldsymbol{y}) \right] \big]_{,j} = 0 \tag{26}$$

which are identical to those encountered in the classical linear elastic homogenization theory. The phase IFPs can be formulated by considering the case where only the inelastic strain coefficient corresponding to mode p in part α is nonzero, yielding

$$\Big[L_{ijkl}(\boldsymbol{y}) \left[-N^{(\alpha,p)}(\boldsymbol{y}) I_{klmn} + h^{(\alpha,p)}_{(k,l)mn}(\boldsymbol{y}) \right] \Big]_{,j} = 0. \tag{27}$$

Periodic boundary conditions are applied on the edges and faces of the microstructural volume, while homogeneous Dirichlet boundary conditions are imposed at the vertices for both Eqs. 26 and 27. It is noteworthy that the phase IFPs are different from the classical EHM due to nonuniformity of the basis functions. Although the IFPs remain linear elastic boundary value problems, the number of required solves increases to $N_{\text{ph}} \times N_{\text{m}}$, compared to only N_{ph} in the original ROM formulation. Previous studies have employed various numerical techniques to solve these IFPs, including the finite element method [28, 56, 57, 58], the generalized finite element method [59], and the reduced spectral method [60].

To illustrate the physical meaning of the higher order basis functions and their effect on the influence functions, deformation of a representative grain α is shown in Figure 2 computed from the phase influence function problem given in Eq. 27. The Figures 2(b)-(e) show the influence functions $h_{i11}^{(\alpha,1)}$, $h_{i11}^{(\alpha,2)}$, $h_{i11}^{(\alpha,3)}$, and $h_{i11}^{(\alpha,4)}$, respectively. The first influence function corresponds to the uniform applied strain mode, which manifests as a uniform expansion (tension) of all finite elements within the grain domain along direction 1. Figure 2(c) shows the effect of the higher-order mode $N^{(\alpha,2)}$, characterized by a transition from compression to tension along direction 1. Similarly, Figures 2(d) and (e) show the actions of modes $N^{(\alpha,3)}$ and $N^{(\alpha,4)}$, which correspond to transitions from compression to tension along directions 2 and 3, respectively. These higher-order modes enable the ROM to capture grain-scale strain gradients and nonuniform deformation patterns that cannot be represented by the uniform mode alone.

2.6 Algorithm

The computational procedure consists of two stages: an offline precomputation stage and an online stage in which the reduced-order system is evolved. The offline stage of the model consists of solving the linear elastic problems shown in Eqs. 26 and 27 using the finite element method. Once the influence functions are obtained, the interaction tensors, $\boldsymbol{P}^{(\beta\alpha,pq)}$, and the localization tensors, $\boldsymbol{A}^{(\beta,p)}$, are precomputed by evaluating Eqs. 13 and 14 using numerical integration.

The online stage involves evolving the microstructural state using the reduced-order system summarized in Box 1. The online stage of the ROM takes macroscale strain increment, $\Delta\overline{\boldsymbol{\varepsilon}}$, together with the state variables from the previous step, and computes the stress coefficients, $\boldsymbol{\sigma}^{(\beta,p)}$, and hardening coefficients, $g^{(\beta,p),s}$. The system is solved using a staggered scheme in which the stresses are obtained via a Newton–Raphson iteration and the hardening variables are updated explicitly, with the two updates iterated until convergence is reached. Newton–Raphson convergence was enforced when $\left\|\boldsymbol{\phi}^{(\beta,p)}\right\|_{\infty} < 10^{-10}$ where $\boldsymbol{\phi}^{(\beta,p)}$ is the residual for grain β and mode s, unless otherwise stated. State-variable convergence was enforced when $\left\|{}_{l+1}^{k+1}\boldsymbol{\sigma}^{(\beta,p)} - {}_{l+1}^{k}\boldsymbol{\sigma}^{(\beta,p)}\right\|_{L_2} < 10^{-5}$

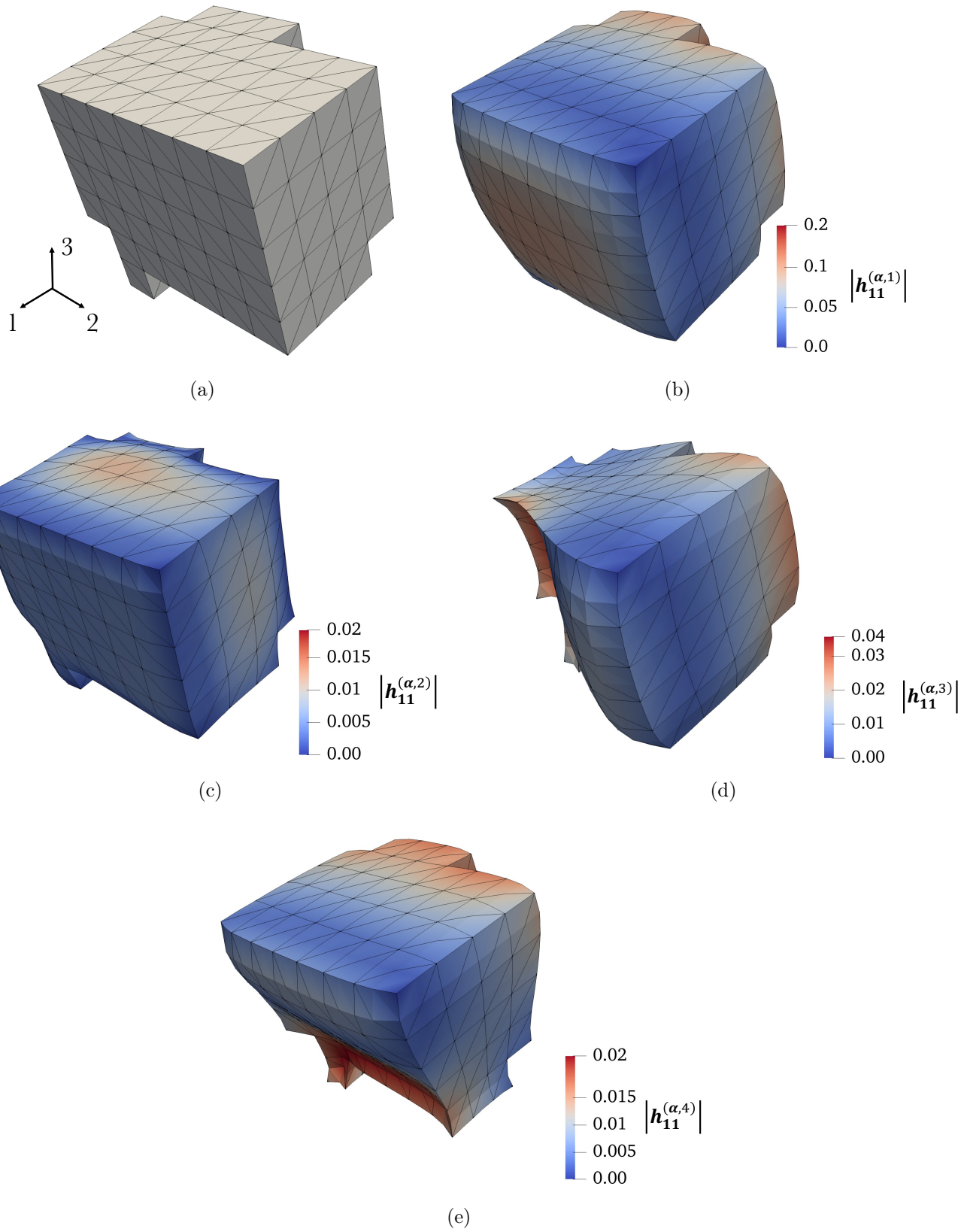

Figure 2: Magnitude of deformation of (a) a single grain within a 10-grain SVE under the application of (b) average mode, $N^{(\alpha,1)}(\boldsymbol{y})$, (c) first mode, $N^{(\alpha,2)}(\boldsymbol{y})$, (d) second mode, $N^{(\alpha,3)}(\boldsymbol{y})$, and (e) third mode, $N^{(\alpha,4)}(\boldsymbol{y})$. The colorbars indicate the deformation magnitude.

Reduced order system of equations:

$$M^{(\beta)}_{klij}\sigma^{(\beta,p)}_{ij} = A^{(\beta,p)}_{klmn}\overline{\varepsilon}_{mn} + \sum_{\alpha=1}^{N_{\rm ph}}\sum_{q=1}^{N_{\rm m}} P^{(\beta\alpha,pq)}_{klmn}\mu^{(\alpha,q)}_{mn} - \mu^{(\beta,p)}_{kl}$$

Flow rule: $\dot{\mu}^{(\beta,p)}_{ij} = \sum_{s=1}^{N_{\rm ss}} \dot{\gamma}^{(\beta,p),s} Z^{(\beta),s}_{ij}$

Slip rate: $\dot{\gamma}^{(\beta,p),s} = \dot{\gamma}_0 \int_{\Theta^{(\beta)}} N^{(\beta,p)}(\boldsymbol{y}) \left[\frac{|\tau^{(\beta),s}(\boldsymbol{y})|}{g^{(\beta),s}}\right]^{1/n} \text{sign}(\tau^{(\beta),s}(\boldsymbol{y}))\, d\boldsymbol{y}$

Hardening rule : $\dot{g}^{(\beta),s} = h_0 \left[\frac{g_{\rm sa}-g^{(\beta),s}}{g_{\rm sa}-g_0}\right] \sum_{r=1}^{N_{\rm ss}} |\dot{\gamma}^{(\beta,1),r}|$

Schmid's law : $\tau^{(\beta),s}(\boldsymbol{y}) = \sum_{q=1}^{N_{\rm m}} N^{(\beta,q)}(\boldsymbol{y})\sigma^{(\beta,q)}_{kl} Z^{(\beta),s}_{kl}$

Box I : Microscale problem for higher order EHM

Given: Macroscopic strain increment $\Delta\overline{\boldsymbol{\varepsilon}}$, the state variables ${}_{l}\boldsymbol{\sigma}^{(\beta,p)}, {}_{l}g^{(\beta,p),s}$ at increment l.

Find: Macroscopic stress, ${}_{l+1}\overline{\boldsymbol{\sigma}}$, and macroscopic tangent moduli, $\dfrac{\partial_{l+1}\overline{\boldsymbol{\sigma}}}{\partial_{l+1}\overline{\boldsymbol{\varepsilon}}}$ at increment $l+1$.

1. Initialize $k \leftarrow 0$, ${}^{k}_{l+1}\boldsymbol{\sigma}^{(\beta,p)} \leftarrow {}_{l}\boldsymbol{\sigma}^{(\beta,p)}$, and ${}^{k}_{l+1}g^{(\beta,p),s} \leftarrow {}_{l}g^{(\beta,p),s}$.

2. Solve for ${}^{k+1}_{l+1}\boldsymbol{\sigma}^{(\beta,p)}$ using Eqs. 28 and 18 together with their derivatives in Eqs. 29 and 30 by Newton-Raphson iterations.

3. Update ${}^{k+1}_{l+1}g^{(\beta,p),s}$ by explicitly integrating the hardening rule (Eq. 16).

4. Check for convergence of ${}^{k+1}_{l+1}\boldsymbol{\sigma}^{(\beta,p)}$ and ${}^{k+1}_{l+1}g^{(\beta,p),s}$.

   If not converged, set $k \leftarrow k+1$ and return to Step 2.

5. Compute the macroscopic tangent moduli, $\dfrac{\partial_{l+1}\overline{\boldsymbol{\sigma}}}{\partial_{l+1}\overline{\boldsymbol{\varepsilon}}}$, using Eq. 33.

6. Compute the macroscopic stress by averaging ${}_{l+1}\overline{\boldsymbol{\sigma}} = \sum_{\beta} c^{(\beta)}\, {}_{l+1}\boldsymbol{\sigma}^{(\beta,1)}$.

Box II : Algorithm for stress update

and $\left\| {}^{k+1}_{l+1}g^{(\beta,p),s} - {}^{k}_{l+1}g^{(\beta,p),s} \right\|_{L_2} < 10^{-5}$, unless otherwise stated. The Newton–Raphson procedure requires evaluating the residual and Jacobian associated with the reduced microscale evolution equations. The residual follows from applying a backward-Euler time discretization to the time derivatives in Eqs. 12 and 18. For grain β and mode p, the residual is given by

$$\phi_{ij}^{(\beta,p)} = M_{ijkl}^{(\beta)} \dot{\sigma}_{kl}^{(\beta,p)} - A_{ijkl}^{(\beta,p)} \dot{\bar{\varepsilon}}_{kl} - \sum_{\alpha=1}^{N_{\mathrm{ph}}} \sum_{q=1}^{N_{\mathrm{m}}} P_{ijkl}^{(\beta\alpha,pq)} \dot{\mu}_{kl}^{(\alpha,q)} + \dot{\mu}_{ij}^{(\beta,p)} \tag{28}$$

where all quantities are evaluated at the next increment, $l+1$. The Jacobian with respect to the reduced stresses is derived as

$$\frac{\partial \phi_{ij}^{(\beta,p)}}{\partial \sigma_{mn}^{(\eta,t)}} = \frac{1}{\Delta t} \delta^{(\beta\eta)} \delta^{(pt)} M_{ijmn}^{(\beta)} - \sum_{q=1}^{N_{\mathrm{m}}} P_{ijkl}^{(\beta\eta,pq)} \frac{\partial \dot{\mu}_{kl}^{(\eta,q)}}{\partial \sigma_{mn}^{(\eta,t)}} + \delta^{(\beta\eta)} \frac{\partial \dot{\mu}_{ij}^{(\eta,p)}}{\partial \sigma_{mn}^{(\eta,t)}} \tag{29}$$

where $\delta^{(\beta\eta)} = 1$ if $\beta = \eta$ and zero otherwise. The derivative $\dfrac{\partial \dot{\boldsymbol{\mu}}^{(\eta,p)}}{\partial \boldsymbol{\sigma}^{(\eta,t)}}$ is obtained from

$$\frac{\partial \dot{\mu}_{ij}^{(\eta,p)}}{\partial \sigma_{mn}^{(\eta,t)}} = \sum_{s} \frac{\partial \dot{\gamma}^{(\eta,p),s}}{\partial \sigma_{mn}^{(\eta,t)}} \; Z_{ij}^{(\eta),s} \tag{30}$$

where the slip-rate derivative is

$$\frac{\partial \dot{\gamma}^{(\eta,p),s}}{\partial \sigma_{mn}^{(\eta,t)}} = \frac{\dot{\gamma}_0}{n} \left[\frac{1}{g^{(\eta),s}} \right]^{1/n} \int_{\Theta^{(\eta)}} N^{(\eta,p)}(\boldsymbol{y}) N^{(\eta,t)}(\boldsymbol{y}) \left[\left| \sum_{q=1}^{N_{\mathrm{m}}} N^{(\eta,q)} \tau^{(\eta,q),s} \right| \right]^{1/n-1} d\boldsymbol{y} \; Z_{mn}^{(\eta),s}. \tag{31}$$

The integral on the right hand side is evaluated on the background finite element mesh when the full model (non-surrogate) is used. Alternatively, when using the surrogate representation of the integral, the slip-rate derivative becomes

$$\begin{aligned} \frac{\partial \dot{\gamma}^{(\eta,p),s}}{\partial \sigma_{mn}^{(\eta,t)}} = \dot{\gamma}_0 \left[\frac{1}{g^{(\eta),s}} \right]^{1/n} & |\tau_{\max}^{(\eta),s}|^{(1/n-1)} \times \\ & \left[\frac{1}{n} I^{(\eta,p)}(\boldsymbol{\tau}_{\mathrm{norm}}^{(\eta),s}) \delta^{(t)} + \frac{\partial I^{(\eta,p)}(\boldsymbol{\tau}_{\mathrm{norm}}^{(\eta),s})}{\partial \tau_{\mathrm{norm}}^{(\eta,t),s}} - \sum_{q=1}^{N_{\mathrm{m}}} \frac{\partial I^{(\eta,p)}(\boldsymbol{\tau}_{\mathrm{norm}}^{(\eta),s})}{\partial \tau_{\mathrm{norm}}^{(\eta,q),s}} \tau_{\mathrm{norm}}^{(\eta,q),s} \delta^{(t)} \right] Z_{mn}^{(\eta),s} \end{aligned} \tag{32}$$

where $\delta^{(t)} = 1$ if $t = t^{\star}$ (i.e., if mode t corresponds to the largest absolute resolved shear stress coefficient) and $\delta^{(t)} = 0$ otherwise. The derivative $\partial I^{(\beta,p)}(\boldsymbol{\tau}_{\mathrm{norm}}^{(\beta),s}) / \partial \tau_{\mathrm{norm}}^{(\beta,q),s}$ can be derived analytically or computed using numerical differentiation methods. For completeness, the macroscale Jacobian

can be obtained by solving the following system of equations

$$\left[\frac{1}{\Delta t}\,\delta^{(\beta\eta)}\delta^{(pq)}M^{(\beta)}_{ijrs} - \sum_{t=1}^{N_{\mathrm{m}}} P^{(\beta\eta,pt)}_{ijmn}\frac{\partial \dot{\mu}^{(\eta,t)}_{mn}}{\partial \sigma^{(\eta,q)}_{rs}} + \delta^{(\beta\eta)}\frac{\partial \dot{\mu}^{(\eta,p)}_{ij}}{\partial \sigma^{(\eta,q)}_{rs}}\right]\frac{\partial \sigma^{(\eta,q)}_{rs}}{\partial \overline{\varepsilon}_{kl}} = \frac{1}{\Delta t}A^{(\beta,p)}_{ijkl}. \tag{33}$$

Once the the system is solved for $\partial\boldsymbol{\sigma}^{(\beta,p)}/\partial\overline{\boldsymbol{\varepsilon}}$, the macroscale tangent modulus can be assembled as $\dfrac{\partial\overline{\boldsymbol{\sigma}}}{\partial\overline{\boldsymbol{\varepsilon}}} = \sum_{\beta=1}^{N_{\mathrm{ph}}} c^{(\beta)}\dfrac{\partial\boldsymbol{\sigma}^{(\beta,1)}}{\partial\overline{\boldsymbol{\varepsilon}}}$ and the updated macroscopic stress is obtained by volume-averaging the updated grain-averaged stress coefficients across all grains. The computational algorithm is summarized in Box 2, where $c^{(\beta)}$ denotes volume fraction of grain β. The algorithm was implemented in Abaqus, and surrogate computations were executed using CalculiX [61], which provided a convenient environment for the required library interfaces.

The total number of stress degrees of freedom in the Step 2 is equal to $N_{\mathrm{m}} \times N_{\mathrm{ph}} \times N_{\mathrm{Voigt}}$, which makes the online stage computationally more expensive than the classical EHM. In the standard EHM formulation, this number reduces to $N_{\mathrm{ph}} \times N_{\mathrm{Voigt}}$ by setting $N_{\mathrm{m}} = 1$. In practice, we observed that the repeated integration of Eq. 19 during each iteration dominates the total computational cost. This is primarily due to the requirement for a refined integration mesh to accurately resolve the high nonlinearity introduced by the large exponent $1/n$ typically used in crystal plasticity flow rules.

The implementation described above establishes the complete computational framework for the proposed reduced-order model. To assess its accuracy and efficiency, a series of numerical experiments were conducted on representative polycrystalline aggregates subjected to various loading conditions. These simulations aim to evaluate the model's ability to reproduce microscale fields, capture intergranular heterogeneity, and predict the macroscopic response in comparison with full-field crystal plasticity finite element simulations.

3 Numerical Experiments

The capabilities of the higher order EHM (HEHM) model are assessed by comparing it to the original EHM model and crystal plasticity finite element (CPFE) simulations. The microstructures used in the numerical analyses were generated using the Neper [62] software. Although Neper generates microstructures with a voxel discretization, each voxel was subsequently and consistently subdivided into exactly six tetrahedral elements as described in Ref. [58]. The crystal orientations were randomly sampled from a uniform distribution and rescaled to the Bunge-Euler angle ranges [0, 360°] × [0, 180°] × [0, 360°]. Property contrast between the phases arises solely from differences in crystal orientations within the polycrystal and the size of the microstructure is set to $10\mu\mathrm{m} \times 10\mu\mathrm{m} \times 10\mu\mathrm{m}$. The grains were modeled as aluminum, with the elastic and viscoplastic properties summarized in

Table 1: Elastic and viscoplastic properties of Aluminum.

C_{11}	C_{12}	C_{44}	g_0	g_{sa}	h_0	n	$\dot{\gamma}_0$
108.2 GPa	61.3 GPa	28.5 GPa	3.7 MPa	30.8 MPa	20.4 MPa	0.05	1 s^{-1}

Table 1. For cubic elasticity, the single-crystal constants C_{11}, C_{12} and C_{44} are reported in Voigt (or Kelvin) notation and are used to construct the fourth-order stiffness tensor, consistent with standard crystal plasticity conventions (see Ref. [63] for example). Aluminum has a face-centered cubic (FCC) structure with twelve slip systems.

For the reduced order model simulations, a single reduced integration linear hexahedral finite element was employed to represent the macroscale domain. The macroscopic domain was subjected to strain-controlled loading with boundary conditions described in the following subsections. At the microscale, periodic boundary conditions were applied on the faces and edges of the polycrystal following the approach described in Ref. [58]. Displacements at the corners of the volume were fixed to eliminate rigid-body motion. For the HEHM simulations, the reduced order basis for inelastic strain and stress fields was constructed from the linear polynomial basis ($N_{\text{m}} = 4$) shown in Eq. 7. For simplicity, piecewise-uniform basis functions were used for the slip system strength, $g^{(\beta),s}$ (see Eq. 16).

The reference CPFE simulations were performed directly on the microstructures using the commercial finite element analysis software, Abaqus [63]. Periodic boundary conditions were considered along the domain boundaries, and a macroscopic strain history was applied as loading using procedures detailed in Ref. [64]. Imposition of the periodic boundary conditions brings the conditions of the CPFE model closer to those considered in the computational homogenization method, alleviating differences induced by boundary effects. Domain discretization in the CPFE simulations was performed using hybrid tetrahedral elements (C3D4H) to mitigate volumetric locking effects, while retaining computational efficiency compared to quadratic tetrahedral elements (C3D10 or C3D10HS) [65].

3.1 Discretization effects

The influence of microscale discretization on the performance of the EHM, HEHM, and CPFE models was examined for a 10-grain polycrystal. Three (coarse, medium and fine) microscale meshes were considered, containing 6,000, 48,000, and 384,000 tetrahedral elements as shown in Fig. 3. For the EHM, the meshes are used only to solve the IFPs. Since EHM employs piecewise-uniform basis functions, numerical integration is not needed to evaluate the constitutive response as discussed in Section 2.3. In the HEHM models, the meshes along with first-order (C3D4) and quadratic

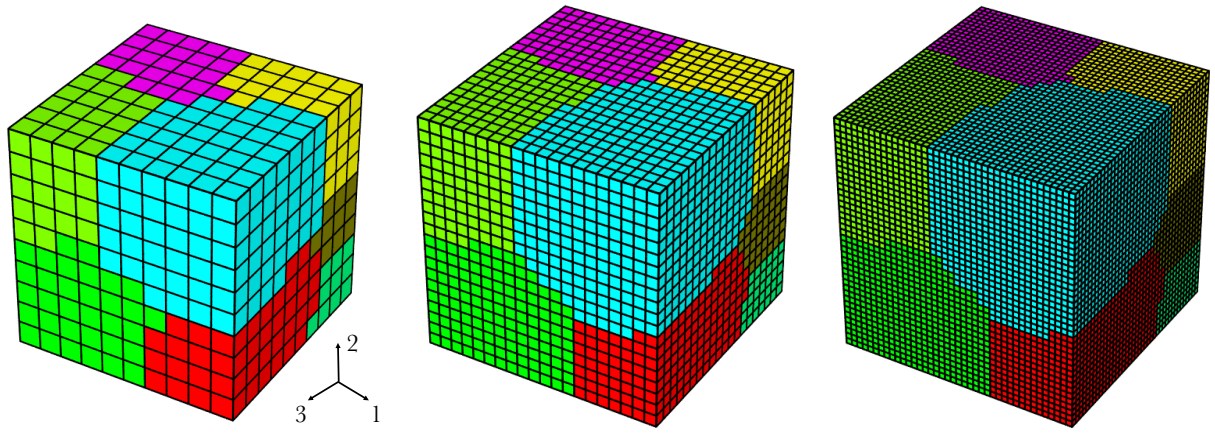

(a) (b) (c)

Figure 3: Generated sample 10-grain microstructure with (a) 1,000, (b) 8,000, and (c) 64,000 voxels.

Table 2: Comparison of EHM, HEHM, and CPFE models in terms of stress at 5% strain, computational time, and speedup.

Method	Element type	# of elements	Stress @ 5% (MPa)	Error (%)	Time (s)	Speedup
EHM	–	6,000	13.1	21.2	18	207.1
EHM	–	384,000	13.1	20.9	16	237.6
HEHM	C3D4	6,000	12.7	17.7	51	73.1
HEHM	C3D4	48,000	12.1	11.7	121	30.8
HEHM	C3D4	384,000	11.7	8.1	667	5.6
HEHM	C3D10	6,000	11.5	6.4	45	82.8
CPFE	C3D4H	6,000	11.0	2.0	206	18.1
CPFE	C3D4H	48,000	10.8	–	233	–

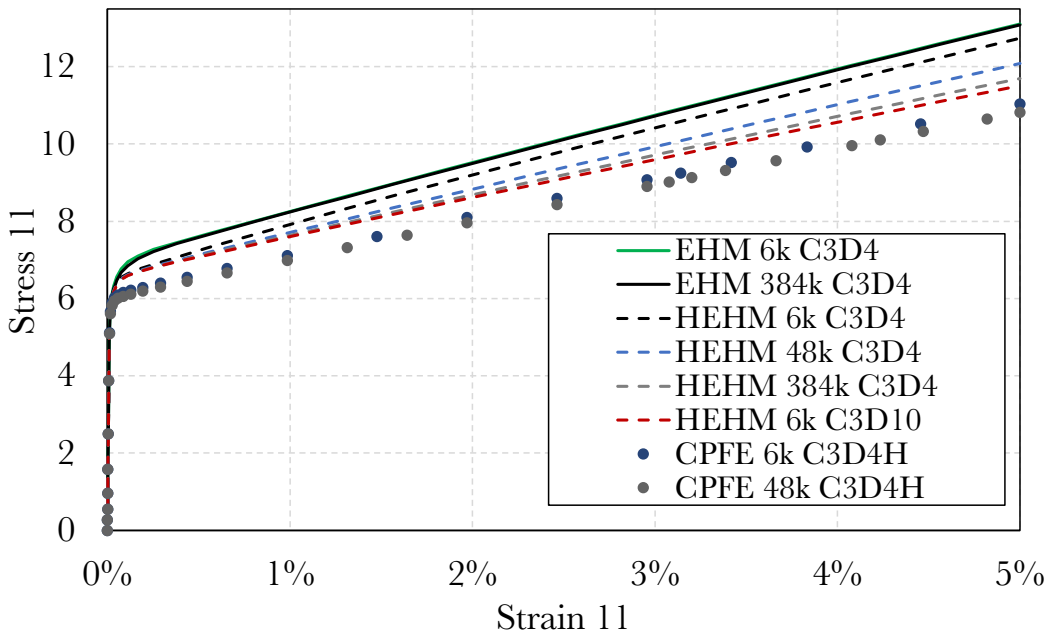

Figure 4: Discretization effects on the performance of EHM, HEHM and CPFE models.

(C3D10) finite elements were used to solve the IFPs, and for numerical integrations. The HEHM simulations employ direct numerical integration of the constitutive model rather than the surrogate based approach. Figure 4 summarizes the overall stress-strain responses of the microstructure when subjected to volume-preserving tensile loading. The response predicted by the EHM is insensitive to mesh refinement as the influence functions are computed with sufficient accuracy using the coarse mesh. In contrast, the HEHM predictions (dashed lines) progressively converge toward the CPFE solutions as the integration grid is refined and higher-order elements (e.g., C3D10) are employed. Meanwhile, the CPFE results obtained using the 6k and 48k meshes (gray and blue markers) exhibit strong agreement, confirming mesh convergence of the reference model.

A quantitative comparison of peak stress error and computational speedup is provided in Table 2. The reported speedup values are computed relative to the CPFE 48k simulation, which was performed in parallel using 16 cores, whereas the rest of the simulations were executed using a single core. The reference CPFE simulation was executed in parallel due to its high computational cost and because direct numerical simulations are typically parallelized, whereas the ROM-based simulations were run serially since the reduced system is small and computationally efficient. The speedup values reported herein are computed by normalizing the ROM wall-clock times to a 16-core equivalent assuming ideal linear scaling, and they should therefore be interpreted as implementation-dependent estimates that may be slightly reduced in practice if parallel efficiency is not perfectly linear. The consistent and monotonic improvement of the HEHM simulations using the C3D4 mesh points to the

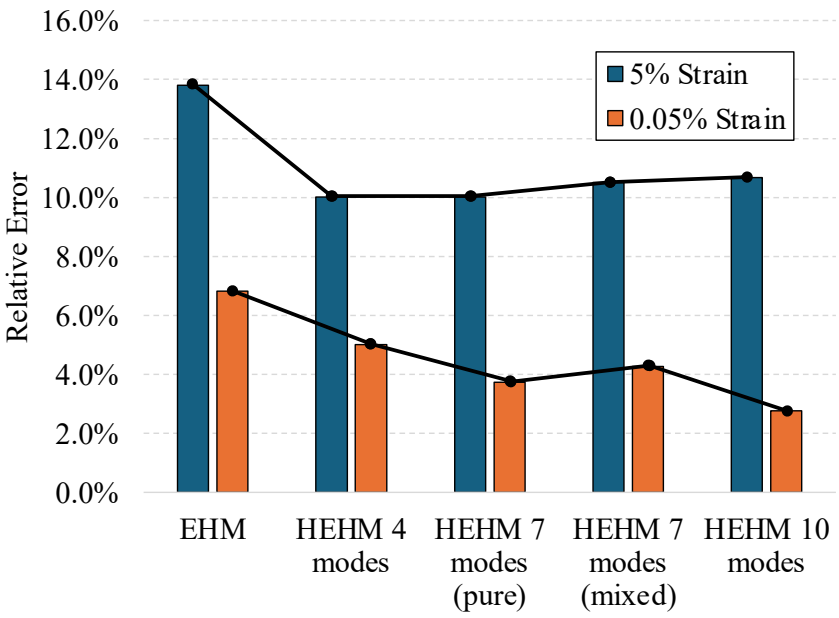

Figure 5: Relative error in the stress (σ_{11}) at onset of plasticity and end of simulation for various number of modes used in the ROM.

importance of the integration accuracy on the overall accuracy of the ROM predictions. However, this comes with a substantial increase in the computational cost when direct numerical integration is employed. Among the tested configurations, the HEHM model with the 6k C3D10 mesh (red dashed line) achieves the most favorable balance between accuracy and computational cost. These results clearly demonstrate that HEHM can systematically reduce the stiffness over-prediction of the classical EHM while maintaining high efficiency. Based on this assessment, the quadratic-element HEHM configuration with approximately 6k elements, corresponding to roughly 24k numerical integration points, is adopted for the subsequent numerical studies.

To examine the effect of increasing the number of modes on the ROM performance, we performed a brief sensitivity study in which the number of modes used in the reduced basis was varied while keeping all other settings fixed. To isolate the effect of basis enrichment on the stress response, the study was conducted without hardening so that additional modal enrichment of hardening-related internal variables is avoided. Figure 5 reports the relative error in σ_{11} at the onset of plasticity (ε=0.05%) and at the end of loading (ε=5%) for the classical EHM and several HEHM configurations with different mode counts. "HEHM 4 modes" employs a 3D linear polynomial basis (constant plus x, y, and z), while "HEHM 10 modes" employs a full 3D quadratic polynomial basis (constant, linear terms, and all quadratic terms). The intermediate cases use seven modes constructed from selected quadratic terms: "HEHM 7 modes (pure)" includes the pure quadratic components x^2, y^2,

and z^2, whereas "HEHM 7 modes (mixed)" includes the mixed quadratic components xy, yz, and zx. Overall, HEHM reduces the stress error compared to EHM at both strain levels, particularly near the onset of plasticity. At the same time, the error does not decrease monotonically with mode count at 5% strain, indicating that the effect of adding higher-order modes can be more intricate than a strictly monotonic improvement across all outputs, and motivating the use of a moderate mode count as a practical choice to balance between accuracy and efficiency.

3.2 Performance study over statistical volume elements (SVEs)

The mechanical response of polycrystalline microstructures varies significantly depending on the grain size distribution, texture, among other statistical morphology parameters. To capture these effects on model performance, we have generated 81 ten-grain statistical volume elements (SVEs) and collectively analyzed the response of approximately 810 grains using EHM, HEHM and CPFE. The microstructures were generated using the grain growth option provided in Neper which results in varying grain shapes and sizes within the SVEs. Grain sizes, defined as equivalent diameter [62], were sampled from a lognormal distribution with mean and standard deviation of 1 μm and 0.35 μm, respectively. Grain sphericity [62] was sampled from a lognormal distribution with mean and standard deviation of 0.145 and 0.03, respectively. Representative SVEs are shown in Figure 6(a–c).

Each SVE was subjected to a strain history corresponding to 5% total strain under volume-preserving uniaxial tension, applied at the rate of 0.05/s. Volume preservation was enforced by prescribing the lateral strain components to satisfy $\varepsilon_{22} = \varepsilon_{33} = -\varepsilon_{11}/2$, thereby maintaining zero macroscopic volumetric strain throughout the loading process. The stress–strain responses ($\overline{\sigma}_{11}$ vs. $\overline{\varepsilon}_{11}$) are plotted in Figure 7. In Figure 7(a), solid lines correspond to the mean response the SVE ensemble predicted by the EHM, HEHM and CPFE simulations, while the shaded regions indicate 2σ confidence intervals, highlighting the uncertainty in the individual SVE within the ensemble. In addition, the dashed and dotted curves explicitly show the corresponding $\mu \pm 2\sigma$ bounds to improve readability when the intervals overlap. The variation from the mean prior to the elastic limit is small, whereas there is a substantial variation after the onset of plastic deformations. The large variation in the elasto-plastic behavior is largely due to the relatively small size of the individual SVEs and relatively high variability in grain morphologies. At 5% strain, the relative errors in the mean stresses computed with EHM and HEHM (compared to CPFE) are 11.81% and 5.39%, respectively. The nearly two-fold reduction in error underscores the improvement achieved by the HEHM. As seen in Figure 7(b), the HEHM model improves predictions starting from the onset of plasticity and throughout the loading history.

Grain-averaged microscale von-Mises stresses were computed for all grains in all SVEs and are

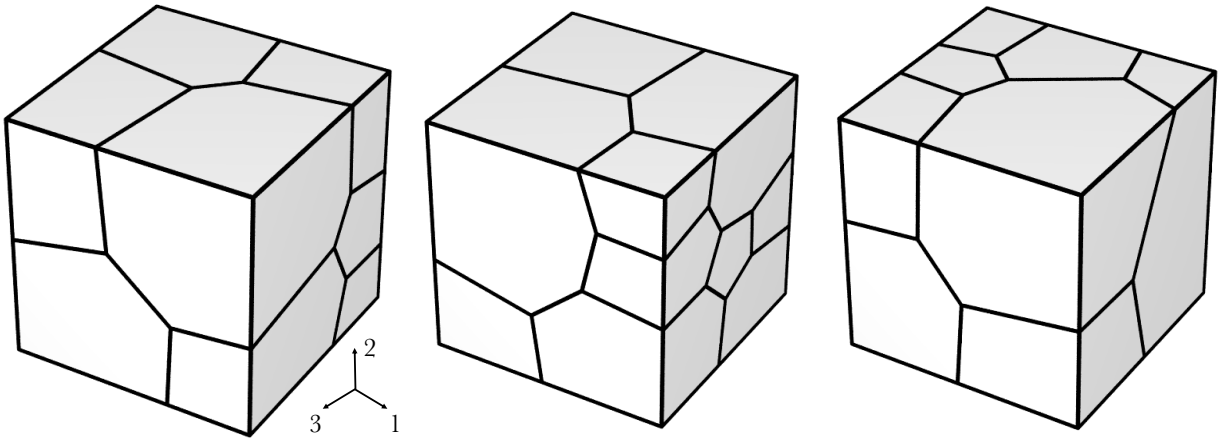

(a) (b) (c)

Figure 6: Generated sample 10-grain SVEs geometries.

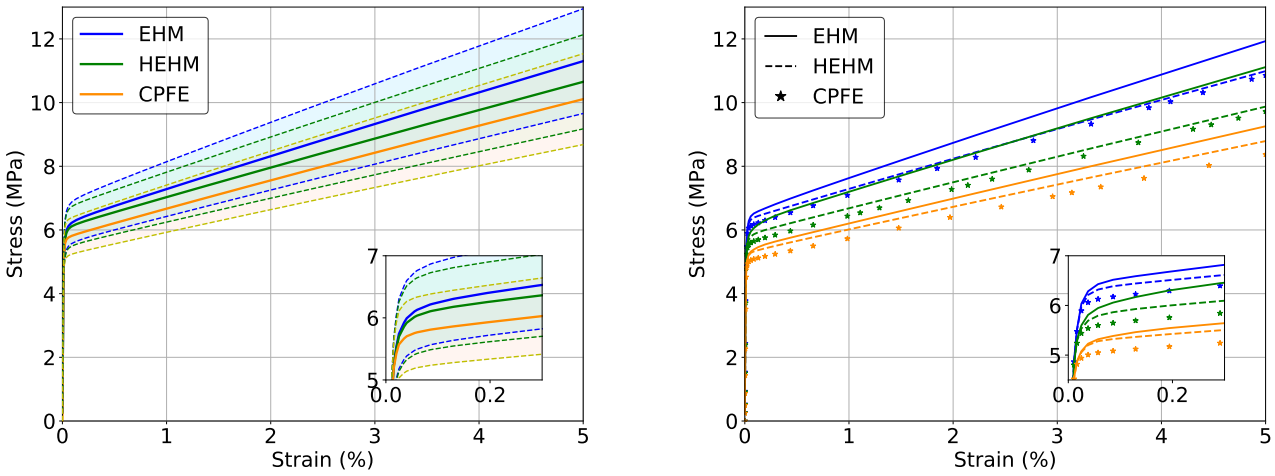

(a) (b)

Figure 7: (a) Means and 2σ confidence intervals for the stress-strain responses of the SVE ensemble, and (b) stress-strain responses of three distinct SVEs from the ensemble. In (b), colors indicate results from the same SVE within the ensemble.

Table 3: Morphological and statistical parameters used to generate SVEs.

Morphology	Grain Size (μm)		Grain Sphericity		Aspect
	Mean	Standard deviation	Mean	Standard deviation	Ratio
Equiaxed	1	0.05	0.145	0.03	(1,1,1)
Elongated	1	0.05	0.145	0.03	(2,1,1)
Low Sphericity	1	0.35	0.3	0.03	(1,1,1)

plotted as a histogram in Figure 8(a). Stress distribution for the EHM model has two peaks at about 16 MPa and 24 MPa. By contrast, stress distributions from HEHM model resembles a unimodal, near-normal distribution similar to the CPFE results. Moreover, the HEHM distribution shows a reduced frequency at the higher stress range compared to the EHM model. Normal distributions were subsequently fitted to the datasets, as shown in Figure 8(b), yielding mean von Mises stresses of 19.7 MPa, 18.6 MPa, and 17.4 MPa for the EHM, HEHM, and CPFE models, respectively. The reduction in the mean stress quantitatively confirms the enhanced predictive capability of the HEHM. Finally, Figure 8(c) plots the relative error between HEHM and CPFE grain-averaged von Mises stresses as a function of normalized grain size. Although grain size is not the sole parameter governing the error, a clear trend of decreasing relative error with increasing normalized grain size can be observed.

3.3 Influence of grain morphology

We further examined the influence of grain morphology by generating ensembles of five 30-grain SVEs. Three cases were considered: (1) equiaxed grains, (2) elongated grains, and (3) low-sphericity grains. The parameters for grain size and grain sphericity (sampled from lognormal distributions) as well as grain aspect ratio used in the three cases are shown in Table 3. The aspect ratio parameter, describing the relative grain dimensions along the 1, 2, and 3 directions, was employed to generate elongated grain morphologies. Figure 9 shows sample morphologies of the SVE ensembles for the three cases considered in this study. In case (1), the SVEs primarily consist of equiaxed grains (Figure 9(a)), whereas in case (2), the grain are equiaxed in 2-3 plane, but are elongated along the 1-direction (Figure 9(b)). The grains in case (3) demonstrate lower sphericity (Figure 9(c)). The histogram of grain shapes in Figure 9(d) shows that SVEs with equiaxed and elongated morphologies have much narrower size distributions compared to those produced using the grain growth model used to generate the 10-grain SVEs. The 10-grain SVEs and those with lower sphericity exhibit considerably broader size distributions.

The mean stress-strain behavior as well as the variability observed under volume-preserving tension loading for the three cases are reported in Figure 10. Comparing the CPFE simulations of the ensembles for the three cases, the mean stress-strain behavior is not significantly affected by the

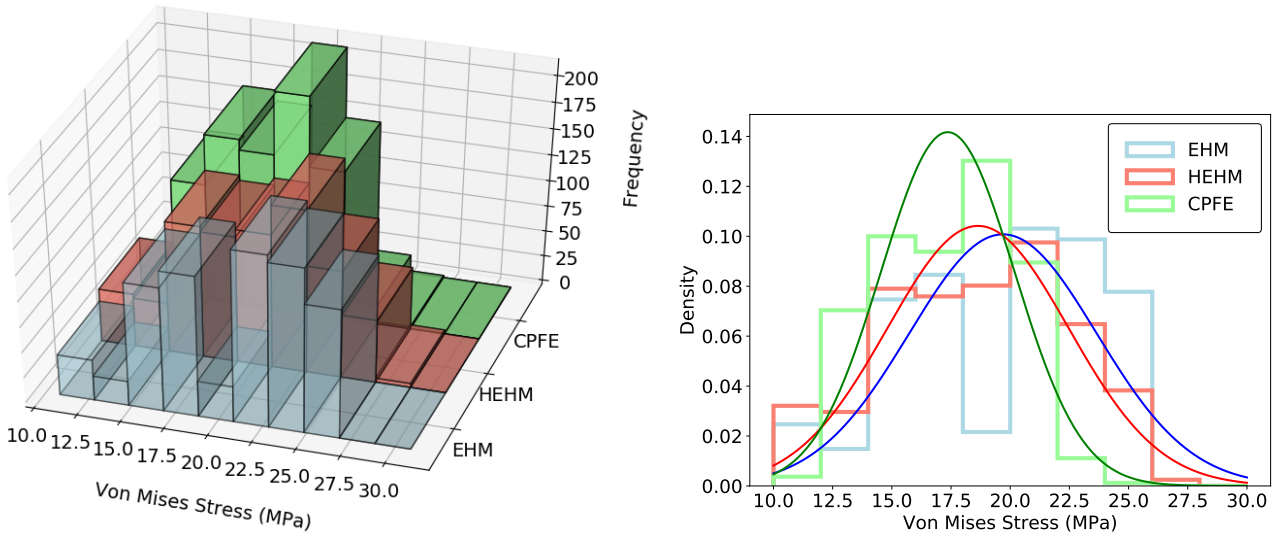

(a) (b)

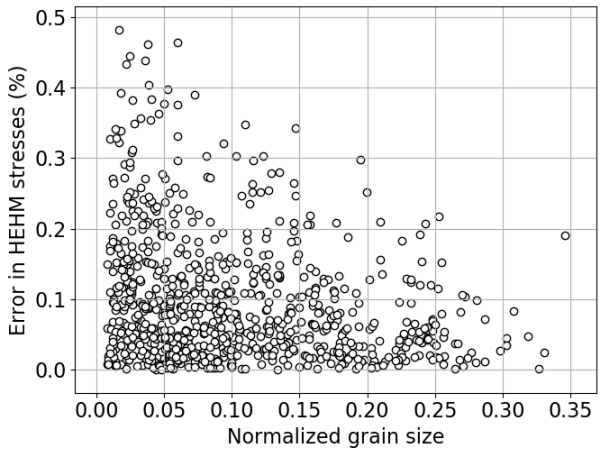

(c)

Figure 8: (a) Histograms of microscale grain-averaged von Mises stresses computed from EHM, HEHM and CPFE models. (b) Normal distributions fitted to the corresponding histograms of grain-averaged von Mises stresses predicted by EHM, HEHM, and CPFE. (c) Relative error between HEHM and CPFE grain-averaged von Mises stresses against normalized grain size.

microstructure morphology. In contrast, the variability in case (3) is noticeably higher compared to the equiaxed and elongated microstructures. This is expected due to the higher variability of grain shape and size in the low sphericity microstructures. The microstructural morphologies do have a significant affect on the performance of the ROMs. The relative errors in the mean stress at 5% strain are 13.68%, 12.39%, and 13.56% for EHM, and 11.85%, 9.97%, and 8.94% for HEHM, for equiaxed, elongated, and lower sphericity SVE ensembles, respectively. The relative error of the classical EHM model does not change as a function of morphology, but there is an observable improvement in the performance of HEHM for case of (3), compared to cases of (1) and (2).

The microscale stress distributions are shown in Figure 11 for a 10-grain polycrystal and in Figure 12 for a 30-grain equiaxed polycrystal. In the 10-grain case, the HEHM solution exhibits larger stress gradients compared to EHM, while for the 30-grain equiaxed polycrystal, the gradients in the HEHM fields are less pronounced. Smaller gradients correspond to lower higher order terms in the field expansions, which may explain the reduced improvement provided by HEHM for equiaxed microstructures.

This observation aligns with intuition from Eshelby's inclusion problem: for nearly spherical inclusions (a subset of ellipsoidal morphologies), the internal fields tend to be more uniform, enabling the original EHM to provide relatively accurate approximations. Overall, the results indicate that grain morphology plays a critical role in the relative performance of HEHM compared to EHM and CPFE. Thus, HEHM may be most beneficial for microstructures with highly irregular morphologies.

3.4 Influence of complex loading conditions

The performance of the HEHM model was further evaluated under several additional loading conditions to assess its generality and robustness. Figure 13a presents the stress–strain response of a 10-grain polycrystal subjected to fully reversed cyclic loading in 1 direction with a stress ratio of $R = -1$. The loading was prescribed as a strain history under a volume-preserving constraint to minimize pressure effects, which would otherwise lead to unrealistically large stresses. The relative errors in peak stress are 18.3% and 4.3% for EHM and HEHM, respectively. The HEHM accurately reproduces the cyclic behavior, exhibiting significantly smaller deviations from the CPFE results compared to the classical EHM.

To examine the rate sensitivity, simulations were conducted at strain rates of 5 s^{-1}, 5×10^{-2} s^{-1}, and 5×10^{-4} s^{-1}, as shown in Figure 13b. Similar to previous sections, volume-preserving tensile loading was considered. The relative errors in peak stress are in the range of $\sim$16% for EHM and $\sim$6% for HEHM. The HEHM consistently delivers improved predictions across all strain rates, demonstrating its robustness with respect to loading rate variations.

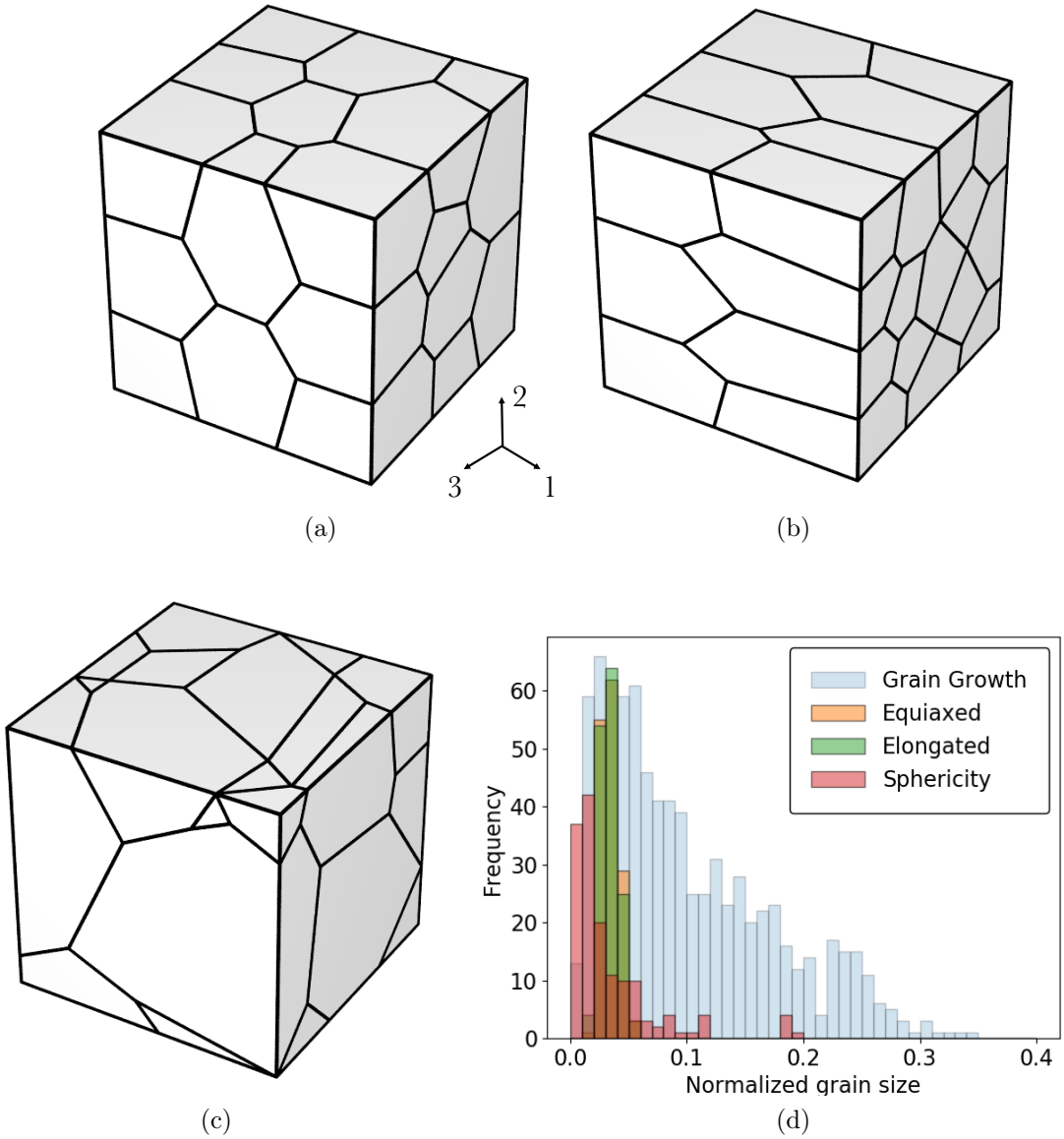

(a) (b) (c) (d)

Figure 9: Sample 30-grain polycrystal with (a) equiaxed, (b) elongated and (c) low sphericity grain morphology. (d) Histogram of grain sizes for grain-growth (10-grain SVEs), equiaxed, elongated, and lower sphericity morphologies.

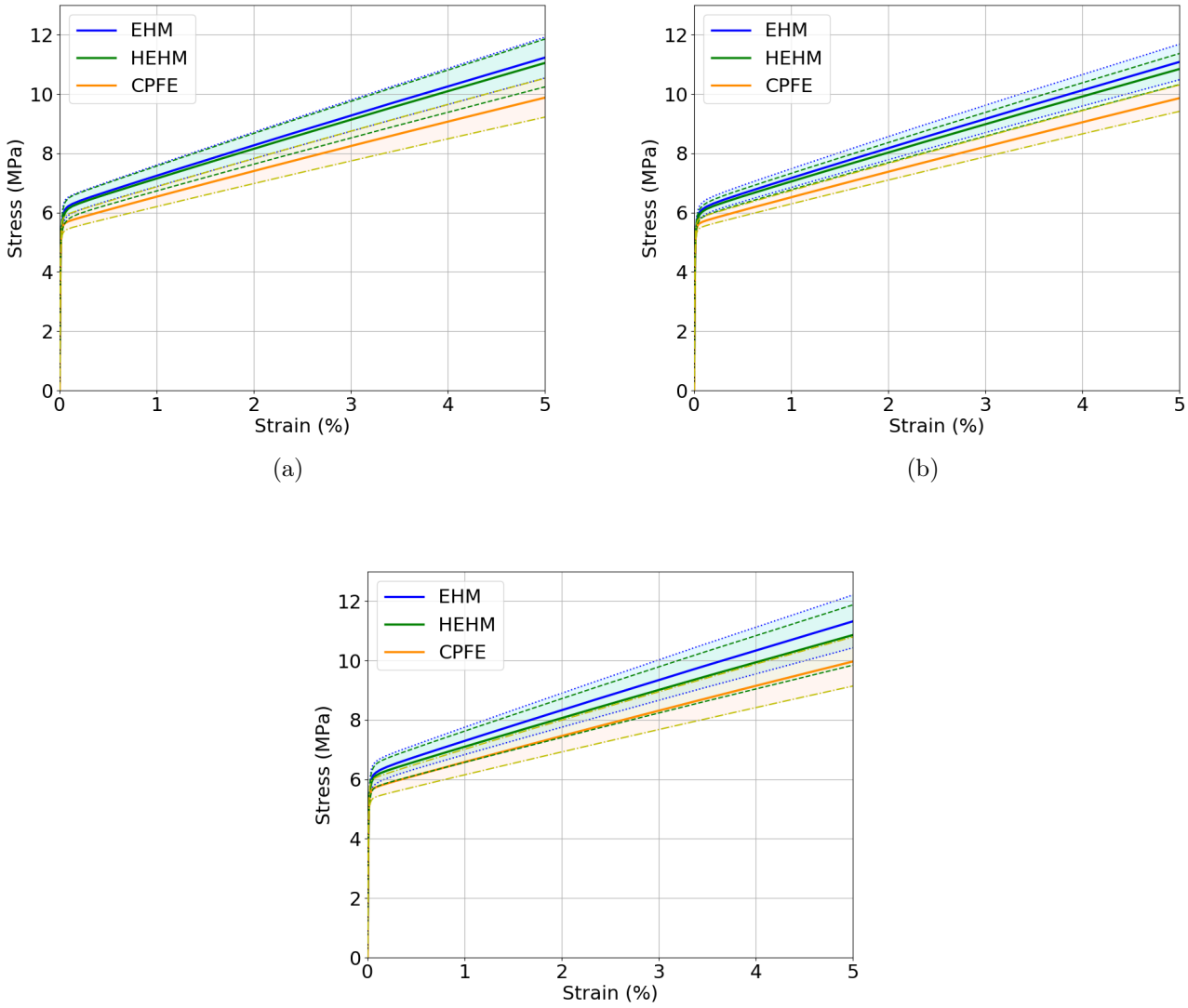

(a)

(b)

(c)

Figure 10: Mean and variance of stress-strain responses of 30 grain polycrystal SVEs under volume-preserving tension with (a) equiaxed, (b) elongated and (c) lower sphericity morphologies.

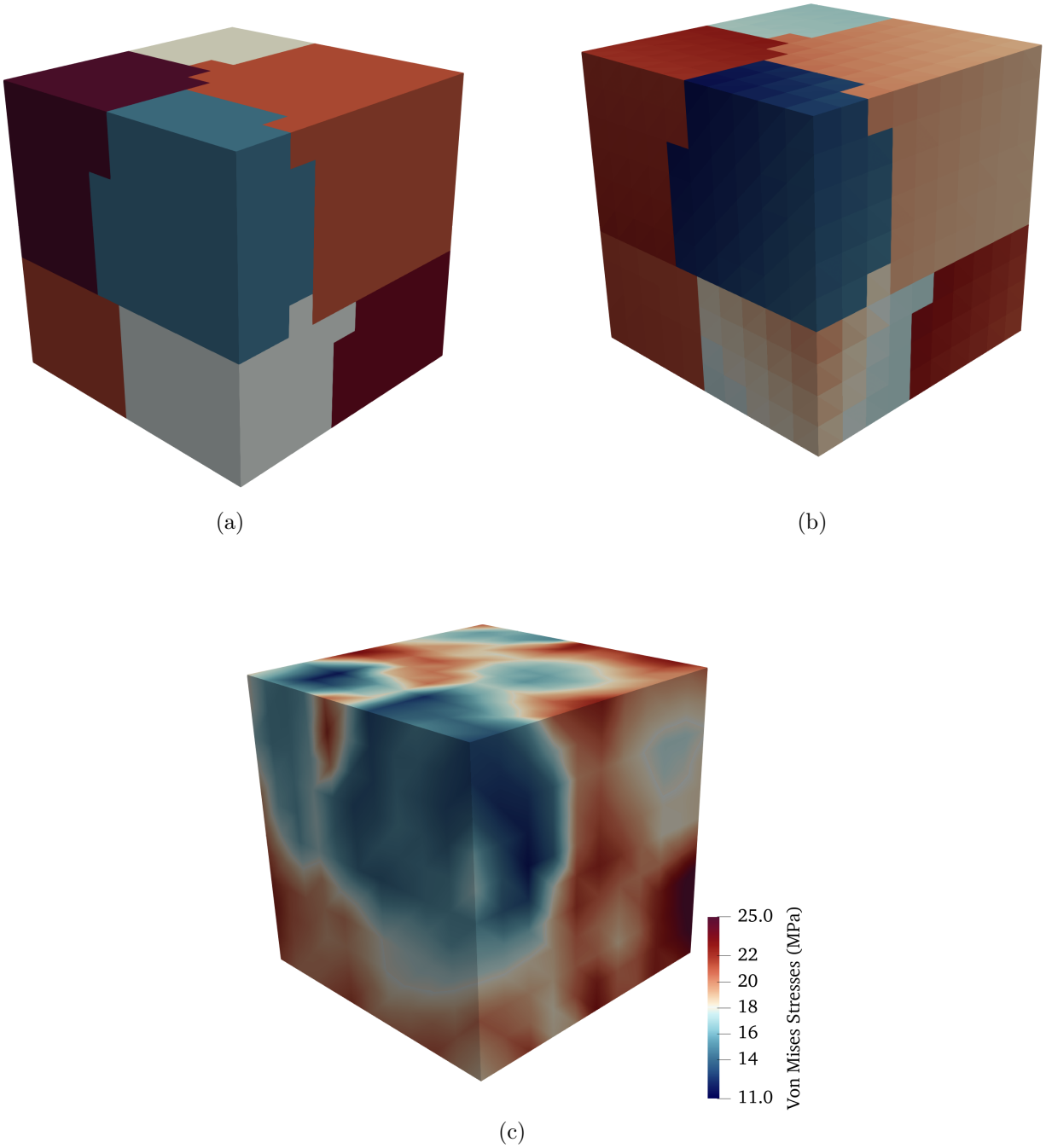

(a) (b)

(c)

Figure 11: Microscale von Mises distribution computed from (a) EHM (b) HEHM (c) CPFE simulations plotted over the 10-grain polycrystal.

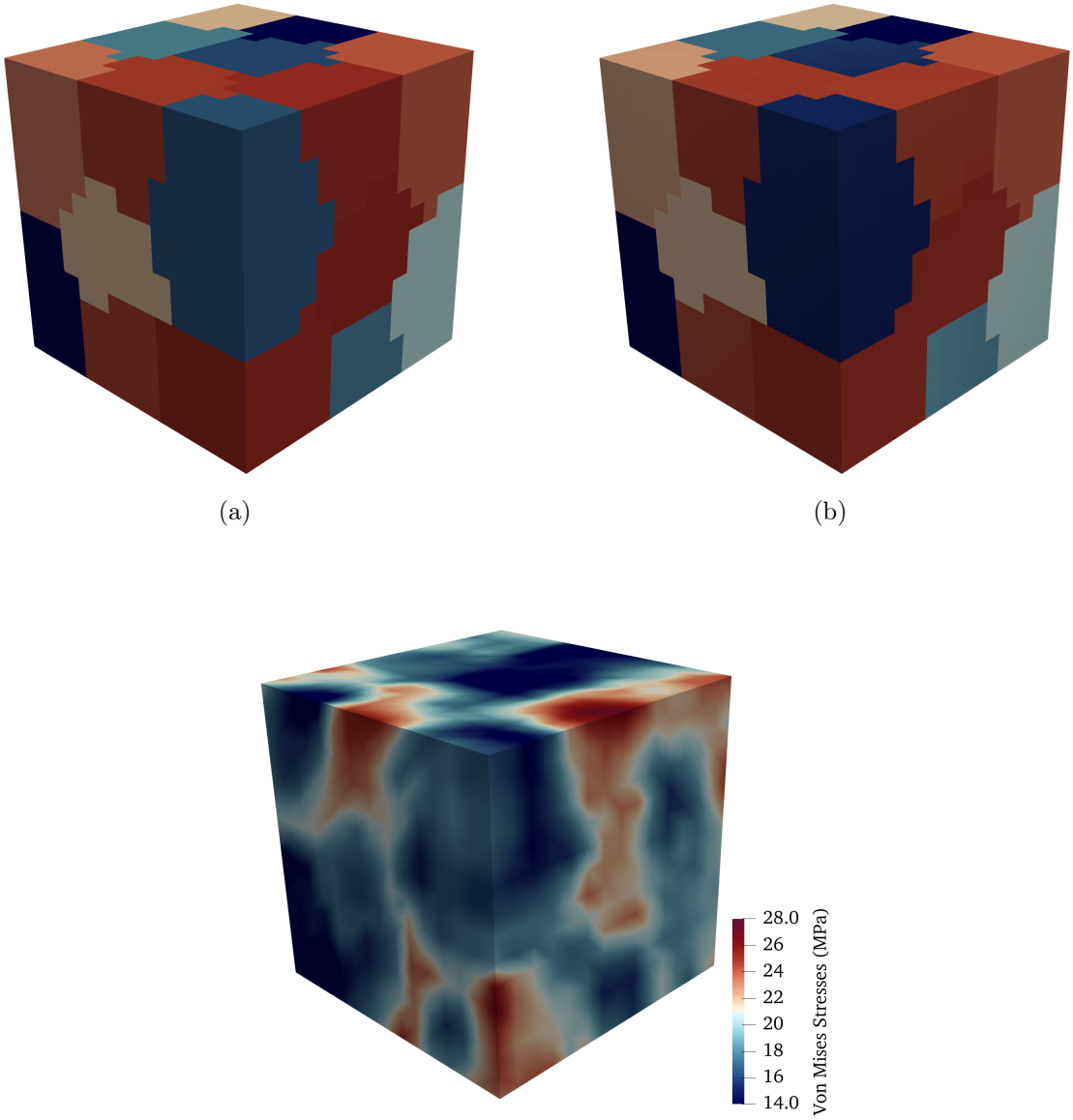

(a) (b) (c)

Figure 12: Microscale von Mises distribution computed from (a) EHM (b) HEHM (c) CPFE simulations plotted over 30-grain equiaxed polycrystal.

Table 4: Strain history applied in the numerical experiment.

Step	$\overline{\varepsilon}_{11}$	$\overline{\varepsilon}_{22}$	$\overline{\varepsilon}_{33}$	$\overline{\varepsilon}_{12}$	$\overline{\varepsilon}_{13}$	$\overline{\varepsilon}_{23}$
1	0.025	0.025	-0.05	0	0	0
2	0.025	0.025	-0.05	0	0	0
3	0.025	0.025	-0.05	0	0	0.05

The model's capability under simple shear was also assessed, with the corresponding results displayed in Figure 13c. The improvement achieved by HEHM is comparable to the previous test cases, with errors in peak shear stress of 8.6% and 2.2% for EHM and HEHM, respectively.

Finally, a complex, multiaxial strain history (summarized in Table 4), consisting of biaxial, volume-preserving tension followed by relaxation and subsequent unidirectional shear, was applied in both ROM and CPFE simulations. The resulting von Mises stress–strain responses are shown in Figure 13d. The HEHM demonstrates notably higher accuracy under shear and significant improvement throughout the full strain history, with errors in peak shear stress of 13.5% and 7.3% for EHM and HEHM, respectively.

Overall, these results confirm that the proposed HEHM framework maintains high accuracy across a broad range of loading paths and strain rates, highlighting its potential as a reliable and general reduced-order model for nonlinear polycrystal plasticity simulations.

3.5 Surrogate model experiments

This section evaluates the efficiency gains achieved by replacing the direct numerical integration of the constitutive model with a surrogate approximation, while ensuring that accuracy remains comparable to the fully integrated solution.

3.5.1 Architecture selection

To construct the surrogate function $I^{(\beta,p)}(\boldsymbol{\tau}^{(\beta)}_{\text{norm}})$ introduced earlier, several neural network architectures were tested, as summarized in Table 5. Three representative cases were considered. The first architecture consisted of a three-layer fully connected network with eight neurons per layer and ReLU activation function. The second architecture used the same layout but replaced ReLU with the ELU activation function, which offers improved smoothness and continuity. The third case was a single-layer perceptron with forty neurons and an activation function defined as

$$f(x) = |x|^{1/n} \operatorname{sign}(x) \tag{34}$$

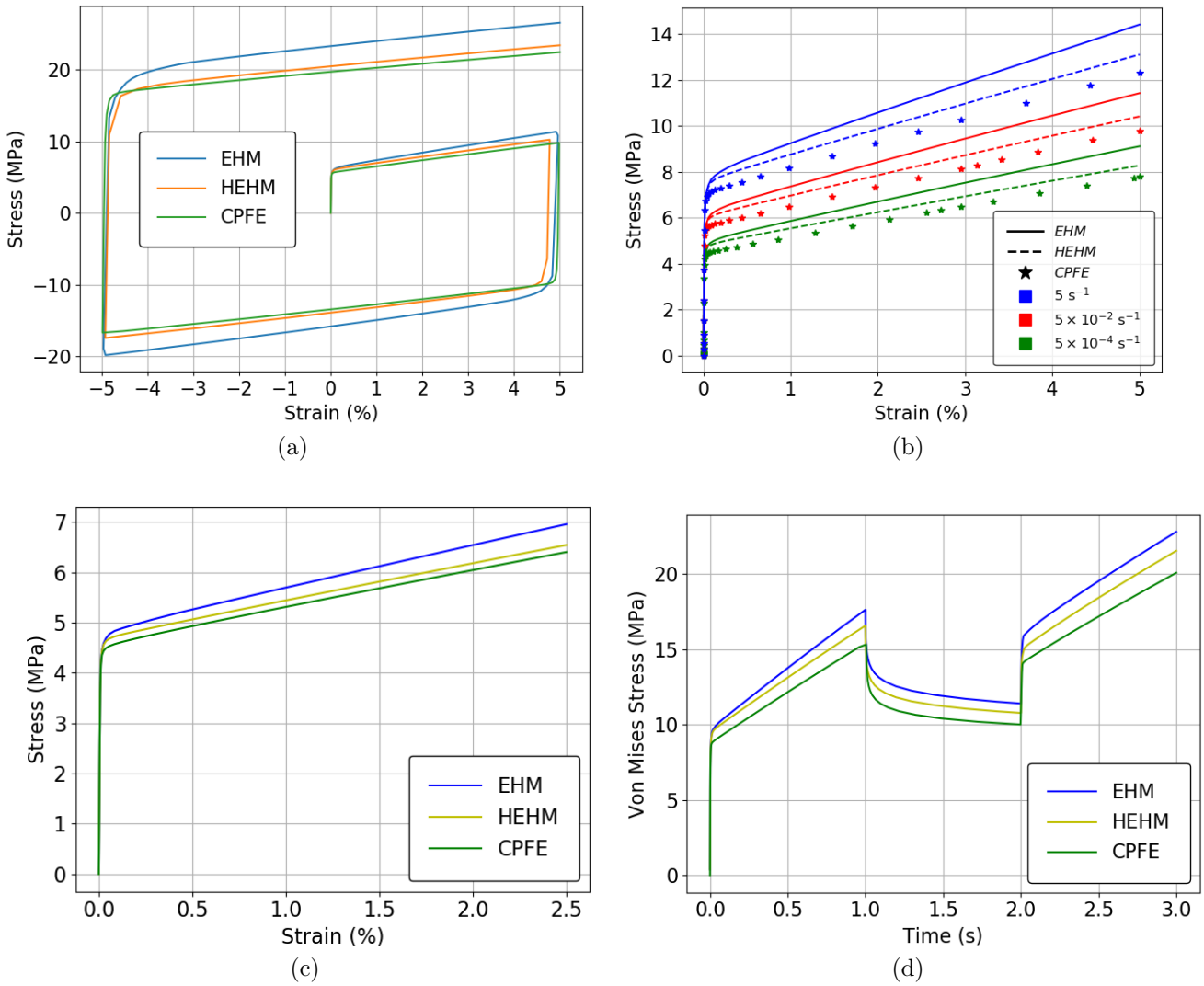

Figure 13: Stress-strain response of a 10-grain polycrystal under (a) cyclical loading, (b) varying strain rates, (c) unidirectional shear, and (d) varying strain history.

Table 5: Loss as a function of the architecture for a single grain.

Case	Activation	Layers	Neurons	RMSE
1	RELU	3	8	1.52×10^{-2}
2	ELU	3	8	3.23×10^{-4}
3	Flow Rule	1	40	3.41×10^{-5}

chosen to mimic the nonlinearity present in the flow rule itself. The biases were set to zero to make sure that integral evaluates to zero at vanishing inputs (i.e., zero slip rate at zero resolved shear stresses). All architectures were designed to contain approximately two hundred trainable parameters so that comparisons would primarily reflect differences in the activation functions rather than differences in model capacity.

Training data was generated by sampling the normalized resolved shear stresses, $\tau_{\text{norm}}^{(\beta,p),s}$, for one representative grain and every mode of the reduced basis. Since after normalization, one of the normalized resolved shear stresses is equal to unity, for every mode p, we fix the mode p at unity and uniformly sample the other modes in the space $[-1,1]^{N_{\text{modes}}-1}$ with 21 points. The networks were trained by initializing with the Nelder-Mead algorithm and refining using BFGS algorithm from the SciPy package [66]. The exact form of the loss function is given by

$$\mathcal{L}^{(\beta,p)} = \frac{||I^{(\beta,p),i} - \overline{I}^{(\beta,p),i}||}{\overline{I}^{(\beta,p),\max}} \tag{35}$$

where $I^{(\beta,p),i}$ is the integral value for input data point i, the $\overline{I}^{(\beta,p),\max}$ is a normalization parameter indicating maximum value of the observed integral. Overline indicates true value of the integral computed from the underlying finite element mesh. Training was performed using a plastic rate sensitivity corresponding to a flow-rule exponent of approximately nine.

The root-mean-square errors (RMSE) between the surrogate predictions and the exact integrals are reported in Table 5. The ReLU-based model exhibits the largest error, likely because the integrand is highly nonlinear and contains sharp transitions that ReLU cannot approximate smoothly. The ELU architecture provides a substantial improvement, indicating that increased smoothness in the activation function is beneficial. The best performance is obtained with the flow-rule-inspired activation, which reduces the RMSE by roughly an order of magnitude relative to the ELU network. These results demonstrate that incorporating physics-based nonlinearities directly into the activation function yields a significantly more accurate surrogate approximation for the reduced integral. The flow-rule inspired activation function is used for the rest of numerical examples below.

Table 6: RMSE between surrogate and reference integral outputs for a single grain as a function of the exponent.

Exponent	RMSE
5	6.18×10^{-6}
9	3.41×10^{-5}
20	1.97×10^{-3}

3.5.2 Effect of the rate parameter

Building on the architectural comparisons presented in the previous subsection, we next examine how the intrinsic nonlinearity of the flow rule influences surrogate accuracy. The nonlinearity is governed by the exponent in the viscoplastic flow rule, and this parameter directly controls the sharpness of the integrand that the surrogate must approximate. To assess this effect, three surrogate models were independently trained using exponents of 5, 9, and 20.

Using the same sampling procedure described in Section 3.5.1, the surrogate-based integral was then evaluated for every mode of a single grain and compared with the corresponding value obtained from direct numerical integration over the background mesh. The resulting RMSE values, summarized in Table 6, reveal a clear trend: lower exponents produce excellent agreement with the reference integrals, while higher exponents introduce significantly sharper nonlinearities that degrade surrogate accuracy. These results highlight the importance of considering the exponent when developing surrogate models for viscoplastic integration, as it fundamentally influences the complexity of the approximation task.

3.5.3 Effect of the grain morphology

The surrogate models trained for a single grain were then used as initial guess and subsequently fine tuned for all grains in a single 10-grain polycrystal. Using the same sampling procedure described in Section 3.5.1, the surrogate-based integral was evaluated for every mode of every grain and compared against the corresponding exact integral computed using the background mesh. A flow-rule exponent of nine was used for this study.

The resulting comparison is shown in Figure 14a. Over the full domain of the outputs ([-1, 1]), surrogate errors are visually negligible. A closer examination near the origin ([-1×10^{-4}, 1×10^{-4}]) reveals small but discernible discrepancies, consistent with the increased sensitivity of the integrand in this region. The computed RMSE of 3.386×10^{-5} aligns with the error scale visible in the inset plot. We further plot comparison between reference and surrogate integral output in Figure 14b. The

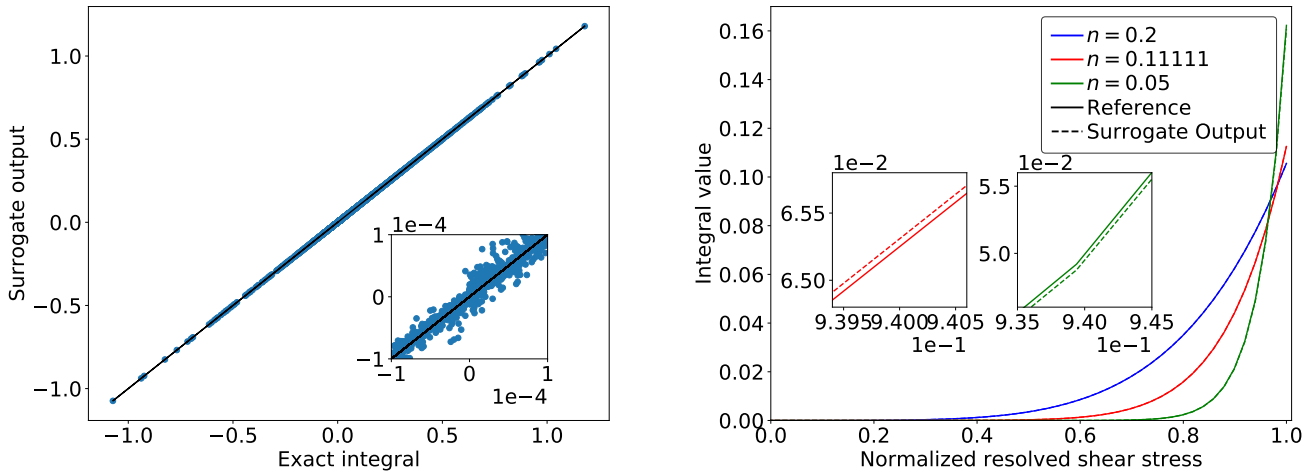

(a) (b)

Figure 14: (a) Truth plot for all grains and modes with inset showing deviations in the proximity of zero and (b) comparison of the reference and surrogate integral values as a function of the normalized resolved shear stress for different exponents.

integral $I^{(\alpha,1)}$ for a representative grain α was evaluated over the full range of $\tau^{(\alpha,1)} \in [-1, 1]$ while remaining components $\tau^{(\alpha,2)}$, $\tau^{(\alpha,3)}$ and $\tau^{(\alpha,4)}$ were fixed at 0.2. Results are shown for exponents of 5, 9, and 20. For the exponent of 5, the surrogate output is nearly indistinguishable from the reference across the entire domain. For exponents of 9 and 20, small deviations become visible upon magnification, with the exponent of 20 requiring less zoom to reveal the discrepancies. It is also noteworthy that the surrogate predictions remain smooth, reflecting the smoothness of the activation functions used in the neural network architecture.

Overall, these results show that the surrogate accurately captures the dominant nonlinear structure of the integrand. Moreover, the surrogate performs consistently across all grains, indicating that the model generalizes effectively across the variations in grain morphology present within the polycrystal.

3.5.4 Accuracy and efficiency study

HEHM combined with surrogate integration model was evaluated for both accuracy and computational efficiency by subjecting a 10-grain polycrystal in tension in 1, 2, and 3 as well as loading it in shear in 12, 23, and 31 directions.

Figure 15 presents the macroscopic stress–strain responses obtained from the HEHM with surrogate-based integration and compares them with the responses from the HEHM using full finite

element integration. For the HEHM simulations with surrogate-based integration, the Newton–Raphson residual tolerance was relaxed to 10^{-2} and the state-variable convergence tolerance was relaxed to 10^{-3} to improve robustness. All simulations and surrogate training were performed using a plastic rate sensitivity of $n = 1/9$ (corresponding to an exponent of approximately nine). Across most loading cases, the surrogate-based HEHM reproduces the fully integrated HEHM response with high fidelity. Only small deviations are observed for case of shear loading in the 31 direction. The offline cost of the HEHM with surrogate approach is comprised of integral data generation and surrogate training. The integral data generation cost is negligible relative to the influence-function solves that dominate the ROM offline stage. In the current prototype, surrogate training is dominated by implementation overhead because the code is serial and not performance-optimized, and it is therefore expected to decrease in an optimized implementation. The associated computational times are reported in Table 7. The reference simulation reported in Table 7 corresponds to the CPFE 6k setup used in Table 2 with the same element type and number of elements. The Table 7 reference timing was obtained using 4 cores, a rate-sensitivity exponent of 9 (instead of 20), and was run on an Intel(R) Core i7-4578U CPU @ 3.00GHz rather than an Intel Xeon Gold compute node. Relative to the reference CPFE simulation, the HEHM with full integration provides roughly a 7× speedup, the surrogate-enhanced HEHM achieves approximately a 70× speedup, and the classical EHM attains nearly a 300× speedup. These results demonstrate that the surrogate integration reduces the computational cost of the HEHM by about an order of magnitude while preserving its accuracy across a broad range of loading conditions. This subsection does not re-quantify HEHM accuracy versus CPFE because that comparison is already established in the preceding three subsections, and instead it focuses on whether the surrogate preserves HEHM accuracy while improving computational efficiency.

It is important to emphasize that the intent of this work is not to advocate for a specific neural-network architecture, but rather to demonstrate a general methodology for constructing surrogate integrators for ROMs with nonuniform basis functions. The architectures examined here serve only as representative examples for evaluating the approach. As shown in Tables 5 and 6, surrogate accuracy inevitably degrades as the flow-rule exponent increases, reflecting the sharper nonlinearities the network must approximate. Consequently, alternative architectures, including deeper networks, different activation functions, or other physics informed formulations, may be more suitable depending on the material system and modeling requirements. The proposed framework is therefore flexible, and the surrogate model may be tailored to specific application without loss of generality.

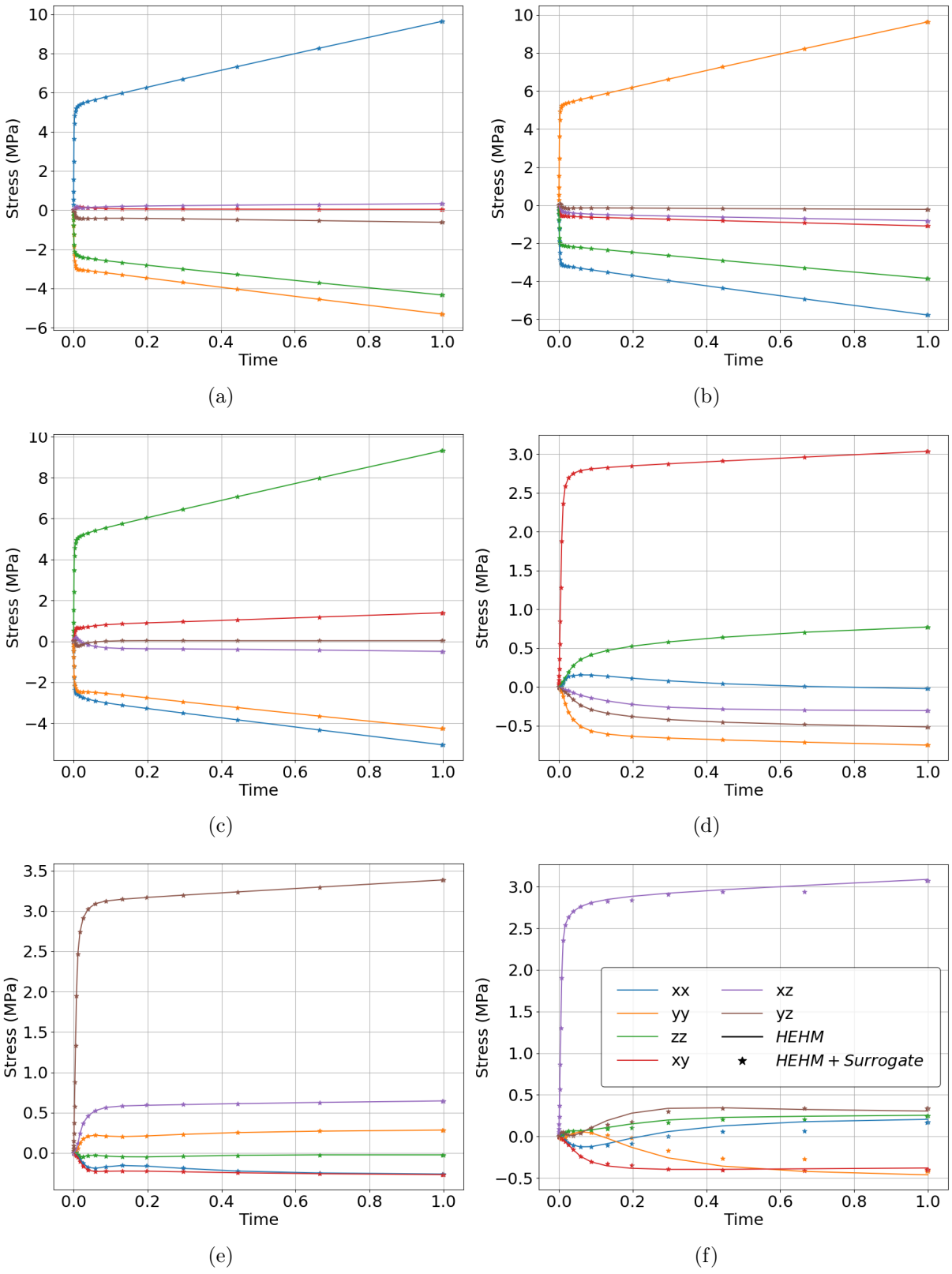

Figure 15: Stress-strain response of 10 grain polycrystal under volume-preserving tension in (a) 1 (b) 2 (c) 3 directions and shear in (d) 12 (e) 23 (f) 31 directions.

Table 7: Comparison of computational time and speedup for different methods, computed for the full 5% strain loading under direction 1.

Method	**Time (s)**	**Speedup**	**Cores**
CPFE	82.89	–	4
HEHM	50.18	6.6	1
HEHM Surrogate	4.78	69.4	1
EHM	0.98	338.0	1

4 Conclusion

This manuscript demonstrated the capabilities of the EHM framework when higher-order basis functions are employed in the model order reduction. The general objective of incorporating the specific type of higher order functions is to achieve consistent and non-trivial (across microstructures and loading conditions) improvement of model accuracy, while retaining the primary function of the ROM, i.e., reduced computational cost. We also presented a surrogate model for the integrals arising from the weak enforcement of the constitutive equations. By introducing normalized coefficients, this surrogate transforms the integration problem into an interpolation problem, achieving an order of magnitude reduction in computational cost without any reduction in integration accuracy.

The performance of the model is demonstrated on low-phase contrast polycrystalline microstructures, accounting for stochastic variations in grain morphology and crystal orientations. The higher-order model consistently exhibits softer mechanical behavior compared to the original EHM, reducing the discrepancy with the reference CPFE simulations. However, the level of improvement depends on grain size and morphology. More specifically, and rather intuitively, the level of improvement is high when the response fields are better approximated with the basis functions being included in the ROM. While more complex basis functions, e.g., those generated by preliminary nonlinear CPFE (training) simulations as typically used in NTFA models could yield better accuracy when loading is similar to the training simulations, the proposed approach guarantees that the prediction accuracy is no less than EHM regardless of loading, but could be improved substantially from this baseline. While the presented results capture stochastic variations in grain morphology and crystal orientations, the scope of this study is limited to low-phase-contrast polycrystalline materials, and extension to higher phase-contrast systems remains a subject of future work.

The key advantage of the HEHM model lies in the enhanced reduced basis without requiring nonlinear simulations during the offline stage, keeping offline costs relatively low. In the online stage, most of the computational cost arises from integrating the constitutive law over a large set of quadrature points. This cost is substantially mitigated by the surrogate model; however, the

surrogate can degrade Newton–Raphson convergence for high plastic rate sensitivities.

CRediT authorship contribution statement

Aslan Nasirov: Conceptualization, Methodology, Software, Formal analysis, Investigation, Data curation, Visualization, Writing – original draft, Writing – review & editing. Caglar Oskay: Conceptualization, Supervision, Methodology, Formal analysis, Writing – review & editing, Project administration, Funding acquisition.

Data availability

Data supporting the findings of this study are available from the corresponding author upon reasonable request.

Declaration of competing interest

The authors declare that they have no known competing financial interests or personal relationships that could have appeared to influence the work reported in this manuscript.

Acknowledgments

The authors gratefully acknowledge the financial support from the National Aeronautics and Space Administration (NASA) Space Technology Early State Innovation (ESI) Grant (No.:80NSSC20K0294). The authors thank the Vanderbilt University Advanced Computing Center for Research and Education (ACCRE) for computational resources.

References

[1] T. Schlick et al. “A Multiscale Vision - Illustrative Applications from Biology to Engineering”. In: *Int. J. Mult. Comp. Eng.* 19 (2021), pp. 39–73.

[2] José Miranda Guedes and Noboru Kikuchi. “Preprocessing and postprocessing for materials based on the homogenization method with adaptive finite element methods”. In: *Computer Methods in Applied Mechanics and Engineering* 83.2 (1990), pp. 143–198. ISSN: 0045-7825.

[3] Thomas J.R. Hughes et al. "The variational multiscale method—a paradigm for computational mechanics". In: *Computer Methods in Applied Mechanics and Engineering* 166.1 (1998). Advances in Stabilized Methods in Computational Mechanics, pp. 3–24. ISSN: 0045-7825.

[4] Yalchin Efendiev and Thomas Y Hou. *Multiscale finite element methods: theory and applications*. Vol. 4. Springer Science & Business Media, 2009.

[5] Thomas Y. Hou and Xiao-Hui Wu. "A Multiscale Finite Element Method for Elliptic Problems in Composite Materials and Porous Media". In: *Journal of Computational Physics* 134.1 (1997), pp. 169–189. ISSN: 0021-9991.

[6] F. Feyel and J.L. Chaboche. "FE2 multiscale approach for modelling the elastoviscoplastic behaviour of long fibre SiC/Ti composite materials". In: *Computer Methods in Applied Mechanics and Engineering* 183 (2000), pp. 309–330.

[7] M. Marino, B. Hudobivnik, and P. Wriggers. "Computational homogenization of polycrystalline materials with the Virtual Element Method". In: *Computer Methods in Applied Mechanics and Engineering* 355 (2019), pp. 349–372. ISSN: 0045-7825. DOI: https://doi.org/10.1016/j.cma.2019.06.004. URL: https://www.sciencedirect.com/science/article/pii/S0045782519303445.

[8] H. Moulinec and P. Suquet. "A numerical method for computing the overall response of nonlinear composites with complex microstructure". In: *Computer Methods in Applied Mechanics and Engineering* 157.1 (1998), pp. 69–94. ISSN: 0045-7825. DOI: https://doi.org/10.1016/S0045-7825(97)00218-1. URL: https://www.sciencedirect.com/science/article/pii/S0045782597002181.

[9] Satyajit Mojumder et al. "Multiscale Modeling of Process-Induced Defects in Fused Filament Fabrication-Printed Materials". In: *Advanced Engineering Materials* n/a.n/a (), p. 2402592. DOI: https://doi.org/10.1002/adem.202402592. eprint: https://advanced.onlinelibrary.wiley.com/doi/pdf/10.1002/adem.202402592. URL: https://advanced.onlinelibrary.wiley.com/doi/abs/10.1002/adem.202402592.

[10] M. Mosby and K. Matouš. "Computational homogenization at extreme scales". In: *Extreme Mechanics Letters* 6 (Mar. 2016). ISSN: 2352-4316. DOI: 10.1016/j.eml.2015.12.009. URL: https://www.osti.gov/biblio/1565430.

[11] G. J. Dvorak and Y. Benveniste. "On Transformation Strains and Uniform Fields in Multiphase Elastic Media". In: *Proceedings: Mathematical and Physical Sciences* 437.1900 (1992), pp. 291–310. ISSN: 09628444. URL: http://www.jstor.org/stable/52199 (visited on 08/22/2022).

[12] G. J. Dvorak. "Transformation field analysis of inelastic composite materials". In: *Proceedings of the Royal Society of London. Series A: Mathematical and Physical Sciences* 437.1900 (1992), pp. 311–327. DOI: 10.1098/rspa.1992.0063. eprint: https://royalsocietypublishing.org/doi/pdf/10.1098/rspa.1992.0063. URL: https://royalsocietypublishing.org/doi/abs/10.1098/rspa.1992.0063.

[13] J.C. Michel and P. Suquet. "Computational analysis of nonlinear composite structures using the nonuniform transformation field analysis". In: *Computer Methods in Applied Mechanics and Engineering* 193.48 (2004). Advances in Computational Plasticity, pp. 5477–5502. ISSN: 0045-7825. DOI: https://doi.org/10.1016/j.cma.2003.12.071. URL: https://www.sciencedirect.com/science/article/pii/S004578250400283X.

[14] J.C. Michel and P. Suquet. "Nonuniform transformation field analysis". In: *International Journal of Solids and Structures* 40.25 (2003). Special issue in Honor of George J. Dvorak, pp. 6937–6955. ISSN: 0020-7683. DOI: https://doi.org/10.1016/S0020-7683(03)00346-9. URL: https://www.sciencedirect.com/science/article/pii/S0020768303003469.

[15] F. Covezzi et al. "Comparison of reduced order homogenization techniques: pRBMOR, NUTFA and MxTFA". In: *Meccanica* 53 (2018), pp. 1291–1312.

[16] F. Fritzen, S. Marfia, and V. Sepe. "Reduced order modeling in nonlinear homogenization: A comparative study". In: *Computers & Structures* 157 (2015), pp. 114–131. ISSN: 0045-7949. DOI: https://doi.org/10.1016/j.compstruc.2015.05.012. URL: https://www.sciencedirect.com/science/article/pii/S0045794915001492.

[17] A. Mishra et al. "Enhanced transformation field analysis for reduced-order modeling of problems with cohesive interfaces". In: *Computer Methods in Applied Mechanics and Engineering* 421 (2024), p. 116755. ISSN: 0045-7825. DOI: https://doi.org/10.1016/j.cma.2024.116755. URL: https://www.sciencedirect.com/science/article/pii/S0045782524000112.

[18] F. Fritzen and M. Leuschner. "Reduced basis hybrid computational homogenization based on a mixed incremental formulation". In: *Computer Methods in Applied Mechanics and Engineering* 260 (2013), pp. 143–154. ISSN: 0045-7825. DOI: https://doi.org/10.1016/j.cma.2013.03.007. URL: https://www.sciencedirect.com/science/article/pii/S0045782513000583.

[19] V. Sepe, S. Marfia, and E. Sacco. "A nonuniform TFA homogenization technique based on piecewise interpolation functions of the inelastic field". In: *International Journal of Solids and Structures* 50.5 (2013), pp. 725–742. ISSN: 0020-7683. DOI: https://doi.org/10.1016/j.ijsolstr.2012.11.005. URL: https://www.sciencedirect.com/science/article/pii/S0020768312004684.

[20] F. Covezzi et al. “Homogenization of elastic–viscoplastic composites by the Mixed TFA”. In: *Computer Methods in Applied Mechanics and Engineering* 318 (2017), pp. 701–723. ISSN: 0045-7825. DOI: https://doi.org/10.1016/j.cma.2017.02.009. URL: https://www.sciencedirect.com/science/article/pii/S0045782516308635.

[21] J. Yvonnet, D. Gonzalez, and Q.-C. He. “Numerically explicit potentials for the homogenization of nonlinear elastic heterogeneous materials”. In: *Computer Methods in Applied Mechanics and Engineering* 198.33 (2009), pp. 2723–2737. ISSN: 0045-7825. DOI: https://doi.org/10.1016/j.cma.2009.03.017. URL: https://www.sciencedirect.com/science/article/pii/S0045782509001492.

[22] Z. Liu, M.A. Bessa, and W. K. Liu. “Self-consistent clustering analysis: An efficient multi-scale scheme for inelastic heterogeneous materials”. In: *Computer Methods in Applied Mechanics and Engineering* 306 (2016), pp. 319–341. ISSN: 0045-7825. DOI: https://doi.org/10.1016/j.cma.2016.04.004. URL: https://www.sciencedirect.com/science/article/pii/S0045782516301499.

[23] C. Oskay and J. Fish. “Eigendeformation-based reduced order homogenization for failure analysis of heterogeneous materials”. In: *Computer Methods in Applied Mechanics and Engineering* 196.7 (2007), pp. 1216–1243. ISSN: 0045-7825. DOI: https://doi.org/10.1016/j.cma.2006.08.015. URL: https://www.sciencedirect.com/science/article/pii/S0045782506002933.

[24] Z. Yuan and J. Fish. “Multiple scale eigendeformation-based reduced order homogenization”. In: *Computer Methods in Applied Mechanics and Engineering* 198.21 (2009). Advances in Simulation-Based Engineering Sciences – Honoring J. Tinsley Oden, pp. 2016–2038. ISSN: 0045-7825. DOI: https://doi.org/10.1016/j.cma.2008.12.038. URL: https://www.sciencedirect.com/science/article/pii/S0045782509000243.

[25] D. Xia and C. Oskay. “Reduced order mathematical homogenization method for polycrystalline microstructure with microstructurally small cracks”. In: *International Journal for Numerical Methods in Engineering* 124.14 (2023), pp. 3166–3190. DOI: https://doi.org/10.1002/nme.7243. eprint: https://onlinelibrary.wiley.com/doi/pdf/10.1002/nme.7243. URL: https://onlinelibrary.wiley.com/doi/abs/10.1002/nme.7243.

[26] C. Oskay, Z. Su, and B. Kapusuzoglu. “Discrete eigenseparation-based reduced order homogenization method for failure modeling of composite materials”. In: *Comput. Meth. Appl. Mech. Engrg.* 359 (2020), p. 112656.

[27] R. D. Crouch and C. Oskay. "Symmetric meso-mechanical model for failure analysis of heterogeneous materials". In: *Int. J. Mult. Comp. Eng.* 8 (2010), pp. 447–461.

[28] X. Zhang and C. Oskay. "Eigenstrain based reduced order homogenization for polycrystalline materials". In: *Computer Methods in Applied Mechanics and Engineering* 297 (2015), pp. 408–436. ISSN: 0045-7825. DOI: https://doi.org/10.1016/j.cma.2015.09.006. URL: https://www.sciencedirect.com/science/article/pii/S004578251500300X.

[29] X. Zhang and C. Oskay. "Sparse and Scalable Eigenstrain-based Reduced Order Homogenization Models for Polycrystal Plasticity". In: *Comput. Meth. Appl. Mech. Engrg.* 326 (2017), pp. 241–269.

[30] D. Xia, X. Zhang, and C. Oskay. "Large-deformation reduced order homogenization of polycrystalline materials". In: *Computer Methods in Applied Mechanics and Engineering* 387 (2021), p. 114119. ISSN: 0045-7825. DOI: https://doi.org/10.1016/j.cma.2021.114119. URL: https://www.sciencedirect.com/science/article/pii/S0045782521004503.

[31] Zeliang Liu, C.T. Wu, and M. Koishi. "A deep material network for multiscale topology learning and accelerated nonlinear modeling of heterogeneous materials". In: *Computer Methods in Applied Mechanics and Engineering* 345 (2019), pp. 1138–1168. ISSN: 0045-7825. DOI: https://doi.org/10.1016/j.cma.2018.09.020. URL: https://www.sciencedirect.com/science/article/pii/S0045782518304729.

[32] P. Krysl, S. Lall, and J. E. Marsden. "Dimensional model reduction in non-linear finite element dynamics of solids and structures". In: *International Journal for Numerical Methods in Engineering* 51.4 (2001), pp. 479–504. DOI: https://doi.org/10.1002/nme.167. eprint: https://onlinelibrary.wiley.com/doi/pdf/10.1002/nme.167. URL: https://onlinelibrary.wiley.com/doi/abs/10.1002/nme.167.

[33] J. Yvonnet and Q.-C. He. "The reduced model multiscale method (R3M) for the non-linear homogenization of hyperelastic media at finite strains". In: *Journal of Computational Physics* 223.1 (2007), pp. 341–368. ISSN: 0021-9991. DOI: https://doi.org/10.1016/j.jcp.2006.09.019. URL: https://www.sciencedirect.com/science/article/pii/S0021999106004402.

[34] D. Xia and C. Oskay. "Proper orthogonal decomposition assisted eigendeformation-based mathematical homogenization method for modeling cracks in 3D polycrystalline microstructures". In: *Comput. Meth. Appl. Mech. Engrg.* 418 (2024), p. 116508.

[35] B. A. Le, J. Yvonnet, and Q.-C. He. "Computational homogenization of nonlinear elastic materials using neural networks". In: *International Journal for Numerical Methods in Engineering* 104.12 (2015), pp. 1061–1084. DOI: https://doi.org/10.1002/nme.4953. eprint: https://onlinelibrary.wiley.com/doi/pdf/10.1002/nme.4953. URL: https://onlinelibrary.wiley.com/doi/abs/10.1002/nme.4953.

[36] Yuan Zhongbo and Poh Leong Hien. "Pre-trained transformer model as a surrogate in multiscale computational homogenization framework for elastoplastic composite materials subjected to generic loading paths". In: *Computer Methods in Applied Mechanics and Engineering* 421 (2024), p. 116745. ISSN: 0045-7825. DOI: https://doi.org/10.1016/j.cma.2024.116745. URL: https://www.sciencedirect.com/science/article/pii/S004578252400001X.

[37] J.L. Chaboche et al. "Towards a micromechanics based inelastic and damage modeling of composites". In: *International Journal of Plasticity* 17.4 (2001), pp. 411–439. ISSN: 0749-6419. DOI: https://doi.org/10.1016/S0749-6419(00)00056-5. URL: https://www.sciencedirect.com/science/article/pii/S0749641900000565.

[38] J. Fish, V. Filonova, and Z. Yuan. "Hybrid impotent–incompatible eigenstrain based homogenization". In: *International journal for numerical methods in engineering* 95.1 (2013), pp. 1–32.

[39] P. A. Sparks and C. Oskay. "Identification of Optimal Reduced Order Computational Models for Failure of Heterogeneous Materials". In: *Int. J. Mult. Comp. Eng.* 11 (2013), pp. 185–200.

[40] Kevin Spilker et al. "Piecewise-uniform homogenization of heterogeneous composites using a spatial decomposition based on inelastic micromechanics". In: *Composite Structures* 295 (2022), p. 115836.

[41] Aslan Nasirov and Caglar Oskay. "An affine formulation of eigenstrain-based homogenization method and its application to polycrystal plasticity". In: *Modelling and Simulation in Materials Science and Engineering* 32.8 (2024), p. 085017.

[42] D. Xia and C. Oskay. "Proper orthogonal decomposition assisted eigendeformation-based mathematical homogenization method for modeling cracks in 3D polycrystalline microstructures". In: *Computer Methods in Applied Mechanics and Engineering* 418 (2024), p. 116508.

[43] Bernardo P. Ferreira, F.M. Andrade Pires, and M.A. Bessa. "Adaptivity for clustering-based reduced-order modeling of localized history-dependent phenomena". In: *Computer Methods in Applied Mechanics and Engineering* 393 (2022), p. 114726. ISSN: 0045-7825. DOI: https://doi.org/10.1016/j.cma.2022.114726. URL: https://www.sciencedirect.com/science/article/pii/S0045782522000895.

[44] Andrew Beel and Jacob Fish. "Solver-free reduced order homogenization for nonlinear periodic heterogeneous media". In: *Computer Methods in Applied Mechanics and Engineering* 425 (2024), p. 116932. ISSN: 0045-7825. DOI: https://doi.org/10.1016/j.cma.2024.116932. URL: https://www.sciencedirect.com/science/article/pii/S0045782524001889.

[45] Stephan Wulfinghoff and Jan Hauck. "E3C for Computational Homogenization in Nonlinear Mechanics". In: *arXiv preprint arXiv:2501.13631* (2025).

[46] Jean-Claude Michel and Pierre Suquet. "A model-reduction approach to the micromechanical analysis of polycrystalline materials". In: *Computational Mechanics* 57 (Mar. 2016). DOI: 10.1007/s00466-015-1248-9.

[47] Masayuki Yano and Anthony T. Patera. "An LP empirical quadrature procedure for reduced basis treatment of parametrized nonlinear PDEs". In: *Computer Methods in Applied Mechanics and Engineering* 344 (2019), pp. 1104–1123. ISSN: 0045-7825. DOI: https://doi.org/10.1016/j.cma.2018.02.028. URL: https://www.sciencedirect.com/science/article/pii/S0045782518301087.

[48] Y. Liu et al. "Experimental and computational study of microstructural effect on ductile fracture of hot-forming materials". In: *Mater. Sci. Eng. A* 724 (2018), pp. 298–323.

[49] Y. Liu et al. "Dislocation density informed eigenstrain based reduced order homogenization modeling: verification and application on a titanium alloy structure subjected to cyclic loading". In: *Modelling Simul. Mater. Sci. Eng.* 28 (2020), p. 025004.

[50] F. Roters et al. "Overview of constitutive laws, kinematics, homogenization and multiscale methods in crystal plasticity finite-element modeling: Theory, experiments, applications". In: *Acta materialia* 58.4 (2010), pp. 1152–1211.

[51] J.R. Rice. "Inelastic constitutive relations for solids: An internal-variable theory and its application to metal plasticity". In: *Journal of the Mechanics and Physics of Solids* 19.6 (1971), pp. 433–455. ISSN: 0022-5096. DOI: https://doi.org/10.1016/0022-5096(71)90010-X. URL: https://www.sciencedirect.com/science/article/pii/002250967190010X.

[52] L. Anand. "Constitutive Equations for the Rate-Dependent Deformation of Metals at Elevated Temperatures". In: *Journal of Engineering Materials and Technology* 104.1 (Jan. 1982), pp. 12–17. ISSN: 0094-4289. DOI: 10.1115/1.3225028. eprint: https://asmedigitalcollection.asme.org/materialstechnology/article-pdf/104/1/12/5513557/12_1.pdf. URL: https://doi.org/10.1115/1.3225028.

[53] E. Voce. "The relationship between stress and strain for homogeneous deformations". In: *Journal of the Institute of Metals* 74 (1948), pp. 537–562.

[54] S. A. Smolyak. "Quadrature and Interpolation Formulas for Tensor Products of Certain Classes of Functions". In: *Soviet Mathematics Doklady* 4 (1963), pp. 240–243.

[55] Sergei Manzhos, Koichi Yamashita, and Tucker Carrington. "Fitting sparse multidimensional data with low-dimensional terms". In: *Computer Physics Communications* 180.10 (2009), pp. 2002–2012. ISSN: 0010-4655. DOI: https://doi.org/10.1016/j.cpc.2009.05.022. URL: https://www.sciencedirect.com/science/article/pii/S0010465509001817.

[56] X. Zhang and C. Oskay. "Sparse and scalable eigenstrain-based reduced order homogenization models for polycrystal plasticity". In: *Computer Methods in Applied Mechanics and Engineering* 326 (2017), pp. 241–269. ISSN: 0045-7825. DOI: https://doi.org/10.1016/j.cma.2017.07.027. URL: https://www.sciencedirect.com/science/article/pii/S004578251730347X.

[57] X. Zhang, Y. Liu, and C. Oskay. "Uncertainty Quantification for Microstructure-Sensitive Fatigue Nucleation and Application to Titanium Alloy, Ti6242". In: *Frontiers in Materials* 9, 897998 (May 2022), p. 897998. DOI: 10.3389/fmats.2022.897998.

[58] A. Nasirov et al. "Achieving high efficiency in reduced order modeling for large scale polycrystal plasticity simulations". In: *Finite Elements in Analysis and Design* 228 (2024), p. 104053. ISSN: 0168-874X. DOI: https://doi.org/10.1016/j.finel.2023.104053. URL: https://www.sciencedirect.com/science/article/pii/S0168874X23001464.

[59] D. R. Brandyberry, X. Zhang, and P. H. Geubelle. "A GFEM-based reduced-order homogenization model for heterogeneous materials under volumetric and interfacial damage". In: *Computer Methods in Applied Mechanics and Engineering* 377 (2021), p. 113690. ISSN: 0045-7825. DOI: https://doi.org/10.1016/j.cma.2021.113690. URL: https://www.sciencedirect.com/science/article/pii/S0045782521000268.

[60] Aslan Nasirov and Caglar Oskay. "A reduced order variational spectral method for efficient construction of eigenstrain-based reduced order homogenization models". In: *International Journal for Numerical Methods in Engineering* 125.18 (2024), e7547.

[61] Guido Dhondt. *The finite element method for three-dimensional thermomechanical applications*. John Wiley & Sons, 2004.

[62] R. Quey and M. Kasemer. "The Neper/FEPX Project: Free / Open-source Polycrystal Generation, Deformation Simulation, and Post-processing". In: *IOP Conference Series: Materials Science and Engineering* 1249.1 (2022), p. 012021. DOI: 10.1088/1757-899X/1249/1/012021. URL: https://dx.doi.org/10.1088/1757-899X/1249/1/012021.

[63] Esteban B Marin. *On the formulation of a crystal plasticity model.* Tech. rep. Albuquerque, NM, and Livermore, CA: Sandia National Laboratories, 2006.

[64] Zheng Yuan and Jacob Fish. "Toward realization of computational homogenization in practice". In: *International Journal for Numerical Methods in Engineering* 73.3 (2008), pp. 361–380.

[65] William G Feather, Hojun Lim, and Marko Knezevic. "A numerical study into element type and mesh resolution for crystal plasticity finite element modeling of explicit grain structures". In: *Computational Mechanics* 67.1 (2021), pp. 33–55.

[66] Pauli Virtanen et al. "SciPy 1.0: Fundamental Algorithms for Scientific Computing in Python". In: *Nature Methods* 17 (2020), pp. 261–272. DOI: 10.1038/s41592-019-0686-2.